Composite Structures 378 (2026) 119897

Contents lists available at ScienceDirect

Composite Structures

journal homepage: www.elsevier.com/locate/compstruct

Toolpath-integrated topology optimization for design of additively manufactured fiber-reinforced structures considering limits on fiber curvature

Janet Wong [a], Emily D. Sanders [a,*], David W. Rosen [a,b,*]

[a] George W. Woodruff School of Mechanical Engineering, Georgia Institute of Technology, Atlanta, GA 30332, USA

[b] Institute for High Performance Computing, Agency for Science, Technology, and Research, 1 Fusionopolis Way, #16-16 Connexis, 138632, Republic of Singapore

ARTICLE INFO

Keywords:
Toolpath-integrated topology optimization
Manufacturing constraints
Local constraints
Continuous fiber-reinforced polymers

ABSTRACT

Topology optimization together with additive manufacturing is a promising approach to design and manufacture fiber-reinforced polymer composite structures with high mechanical efficiency attributed to geometrically complex fiber layouts. Nevertheless, structural performance is often degraded in transitioning from design to manufacturing when fiber toolpaths are generated in post-processing with properties that do not match those used during design. We propose a density-based topology optimization formulation for volume-constrained compliance minimization that not only enforces manufacturing-specific local fiber curvature constraints to reduce deviations between as-designed and as-manufactured fiber layouts, but that also integrates a toolpath generation step into each optimization iteration such that mechanical properties associated with as-manufactured fiber–matrix distributions are considered during design. Fiber orientation design variables are defined at support points of radial basis functions so that the curl field associated with the fiber orientations can be expressed as differentiable functions and used to impose the local fiber curvature constraints. To define the fiber–matrix layout concurrently with the design iterations, a two-term truncated Fourier series representation of the fiber orientation design variable field is projected onto a fiber–matrix composite microstructure with finite length scale, and mechanical properties of fiber and matrix are considered directly in the analysis. Several design examples are provided to illustrate how curl constraints can be controlled to meet process-specific fiber curvature limits, how parameters of the Fourier series and projection operation can be tuned to achieve process-specific fiber–matrix distributions, and how the optimized topology, geometry, and fiber layout change when such constraints and parameters are varied.

1. Introduction

Topology optimization has been explored in recent years for design of continuous fiber reinforced polymer (CFRP) composite structures since it leads to designs that can make full use of the design complexity afforded by additive manufacturing (AM) technologies and enhances structural efficiency. In density-based topology optimization of CFRP composite structures, local fiber orientation is typically represented by a discrete vector field and the continuous fiber toolpaths are established in a post-processing step according to the fiber orientation field (e.g., stripe pattern algorithms [1], streamline methods [2,3], projection methods [4,5]) or some other physical quantity (e.g., stress trajectories [6]). These post-processing strategies for fiber toolpath generation can significantly alter the expected local CRFP mechanical properties and lead to reduced structural efficiency of the manufactured CFRP composite structure relative to that predicted during topology optimization. Additionally, manufacturing constraints on fiber toolpath curvature and spacing are typically unaccounted for during topology optimization and exacerbate deviations in mechanical properties between the as-designed and as-manufactured parts. To mitigate the effects of post-processing on mechanical behavior, we present a density-based topology optimization formulation for design of CFRP composite structures that attempts to consider mechanical properties of the as-manufactured part during the optimization iterations by (1) considering mechanical properties associated with the as-manufactured fiber–matrix distribution according to process-specific fiber toolpaths generated in each optimization iteration (i.e., without using homogenized mechanical properties) and (2) enforcing manufacturing constraints on fiber layout that reduce deviations of fiber layout

* Corresponding authors.
E-mail addresses: emily.sanders@me.gatech.edu (E.D. Sanders), rosendw@a-star.edu.sg (D.W. Rosen).

https://doi.org/10.1016/j.compstruct.2025.119897
Received 14 August 2025; Received in revised form 1 November 2025; Accepted 25 November 2025
Available online 2 December 2025

in the as-manufactured part relative to that prescribed by the design algorithm [7].

Toolpath-integrated topology optimization for design of CFRP composite structures has been explored in moving morphable components (MMC) and level-set-based topology optimization, where an explicit representation of continuous fiber paths reduces post-processing efforts and facilitates enforcing manufacturing constraints. However, existing MMC and level-set approaches consider homogenized properties of the CFRP, which means that the length scales of the matrix and fiber materials must be selected appropriately in post-processing to prevent deviations in mechanical behavior between the as designed and as-manufactured parts [8–13]. By using homogenized properties, the ability to tailor the fiber–matrix distribution to a specific manufacturing process is severely limited.

Recent density-based approaches in which the fiber–matrix distribution is explicitly modeled have the potential to avoid the physical restrictions associated with the separation of scales assumption of homogenization [14,15], although this point has not been thoroughly investigated. Ren et al. [15] integrated a fiber toolpath generation algorithm directly into their density-based topology optimization iterations using a strategy similar to dehomogenization of other multi-scale topology optimized structures [16,17]. They projected a truncated Fourier series representation of the fiber orientation design field onto a fiber–matrix composite microstructure with finite length scale in each optimization iteration. The wave projection strategy is particularly amenable to integration into a topology optimization workflow because the Fourier series representation ensures C^1 continuity of the fiber toolpaths and facilitates gradient-based methods to solve the optimization problem. We adopt the wave projection-based approach to fiber toolpath integration pursued by Ren et al. [15] and show how parameters of the wave projection operations can be used to tailor the fiber–matrix distribution of a towpreg to a particular AM process. Importantly, we modify the formulation so that it is amenable to inclusion of manufacturing constraints by defining fiber orientation design variables at support points of compactly supported radial basis functions (CS-RBFs), which allows the manufacturing constraints to be defined as continuous functions of the orientation design variables.

Manufacturing constraints considered here focus on limiting fiber curvature. The maximum allowable local fiber curvature is related to the smallest fiber turning radius that will not cause significant defects such as out-of-plane fiber buckling and tow wrinkling, where the turning radius is limited by the width of the tow, the bending stiffness of the fibers, and limitations associated with the manufacturing equipment itself (e.g., length of links of the robotic arms and position of joints to prevent collision with the arms). In level-set-based topology optimization, curvatures of the fiber paths can be obtained by taking the second derivative of the level set functions [18–20]. A continuous mathematical representation of curvature needed for imposing curvature limits is not as straightforward in density-based topology optimization, where the fiber paths are interpreted from a discrete vector field of fiber orientations. Previous studies indirectly limited fiber curvature by imposing a blurring filter on the orientation design variables [21,22], but this approach does not ensure that precise, practical manufacturing constraints related to curvature are satisfied. Instead, we enforce constraints on the out-of-plane component of the curl of the fiber orientation design variable field to indirectly control local curvature of the fiber tows [7,23]. As in the author's previous work, the fiber orientation design variables are defined at the support points of CS-RBFs to ensure C^1 continuity of the curl field and to facilitate the use of analytical derivatives [7]. Additionally, we use an augmented Lagrangian (AL) method [24,25] to handle the large number of local curl constraints.

The remainder of the paper is organized as follows: Section 2 presents the toolpath-integrated topology optimization formulation for volume-constrained compliance minimization of two-dimensional (2D), single ply CFRP composite structures considering constraints on structure volume and local fiber curvature. Sections 6 and 7 provide details of the AL method and sensitivity analysis, respectively. We show several 2D examples in Section 8, including a study on how parameters of the Fourier series and projection operation can be tailored for different CFRP manufacturing techniques (e.g., automated fiber placement (AFP) and material extrusion (MEX)) and how the associated designs depend on the choice of parameters. As part of the numerical examples, we also compare the results obtained using the proposed toolpath-integrated formulation to those obtained with fiber toolpath generation as a post-processing step. Finally, we conclude the paper in Section 9 with some remarks and discussion on future work.

2. Problem formulation

We consider compliance minimization of CFRP composite structures with constraints on composite volume, fiber volume, and fiber path curvature. The formulation shares several similarities to the authors' prior work [7], but a key distinction is that rather than considering homogenized properties of the fiber–matrix composite material, we characterize mechanical properties of the composite structure from the design variables in each optimization iteration by performing a toolpath generation step to define a fiber–matrix layout with finite length scale. The problem is formulated as,

$$
\begin{aligned}
\min_{\substack{\mathbf{z}\in[0,1]^N \\ \hat{\boldsymbol{\theta}}\in\left[-\frac{\pi}{2},\frac{\pi}{2}\right]^M}} \quad & f(\mathbf{z},\hat{\boldsymbol{\theta}}) = \mathbf{F}^T\mathbf{u}(\mathbf{z},\hat{\boldsymbol{\theta}}) \\
\text{s.t.} \quad & {}^{v}g(\mathbf{z}) = \frac{\sum_{\ell=1}^{N} A_\ell y_\ell}{\sum_{\ell=1}^{N} A_\ell} - v_{\text{all}} \le 0 \\
& {}^{v_f}g(\mathbf{z},\hat{\boldsymbol{\theta}}) = \frac{\sum_{\ell=1}^{N} A_\ell y_\ell \hat{\chi}_\ell}{\sum_{\ell=1}^{N} A_\ell} - v_{\text{all}}^{f} \le 0 \\
& {}^{\zeta}g_\ell(\hat{\boldsymbol{\theta}}) = \zeta_\ell^2(\boldsymbol{\theta}) - \zeta_{\text{all}}^2 \le 0, \quad \ell = 1,\dots,N \\
\text{with} \quad & \mathbf{K}(\mathbf{z},\hat{\boldsymbol{\theta}})\mathbf{u}(\mathbf{z},\hat{\boldsymbol{\theta}}) = \mathbf{F},
\end{aligned}
\tag{1}
$$

where the objective function, $f(\mathbf{z},\hat{\boldsymbol{\theta}})$, is a measure of structural compliance and the mechanical response of the system is defined via the discretized state equations of static elasticity, where $\mathbf{K}(\mathbf{z},\hat{\boldsymbol{\theta}})$, $\mathbf{u}(\mathbf{z},\hat{\boldsymbol{\theta}})$, and $\mathbf{F}$ are the global stiffness matrix, displacement vector, and external load vector, respectively. The design and analysis discretizations are chosen to coincide and a design point is defined at the centroid of each of the N finite elements used in the finite element analysis. The design variables, $\mathbf{z}\in[0,1]^N$, represent the density of composite material at each of the N design points in the design domain, where $z_\ell = 0$ indicates void and $z_\ell = 1$ indicates existence of material at design point ℓ. The design variables, $\hat{\boldsymbol{\theta}}\in\left[-\frac{\pi}{2},\frac{\pi}{2}\right]^M$, represent the local fiber orientation at each of the M support points of compactly supported radial basis functions (CS-RBFs) defined in the design domain, which are projected to the design points to define $\boldsymbol{\theta}\in\left[-\frac{\pi}{2},\frac{\pi}{2}\right]^N$. In (1), the global constraint functions, ${}^{v}g(\mathbf{z})$ and ${}^{v_f}g(\mathbf{z},\hat{\boldsymbol{\theta}})$[1] limit the total volume of composite material and fiber material, respectively, according to the volume fraction limits, v_{all} and v_{all}^{f}, where A_ℓ is the volume of the domain associated with design variable, z_ℓ. The local constraint functions, ${}^{\zeta}g_\ell(\hat{\boldsymbol{\theta}})$, $\ell = 1,\dots,N$, limit the out-of-plane component of the curl of the fiber orientation field, $\hat{\boldsymbol{\theta}}$, according to curl limit, ζ_{all}, as a means to control fiber path curvature. The expression for the out-of-plane component of curl, $\zeta_\ell(\boldsymbol{\theta})$, at design

[1] As shown in Sections 3 and 4, we can only approximately control the fiber volume fraction, v_f, with parameters of the wave projection, and small deviations from the expected v_f may occur. The fiber volume constraint introduced here ensures v_f is consistent with that expected from the wave projection parameters, which is especially important to ensure a fair comparison with structures designed using different curl limits (or no curl limits).

point, ℓ, is defined in Section 5. Variables, $\mathbf{y}$ and $\hat{\chi}$ appearing in (1) are introduced in a series of operations needed to translate the density and orientation design variable fields into stiffness and volume properties of the structure, as described below.

First, to ensure regularity of solutions and a minimum length scale on the structural features, we apply a linear density filter of radius, R, on the density design variables to obtain filtered densities, $\mathbf{y} = \mathbf{P}\mathbf{z}$, where $\mathbf{P}$ is a regularization map with coefficients,

$$P_{ij} = \frac{w_{ij} A_j}{\sum_{k=1}^{N} w_{ik} A_k}, \quad w_{ij} = \max\left[0, \left(R - \|\boldsymbol{x}_i - \boldsymbol{x}_j\|_2\right)\right], \tag{2}$$

and $\|\boldsymbol{x}_i - \boldsymbol{x}_j\|_2$ is the Euclidean norm between the centroids of elements i and j [26,27]. Next, we use a solid isotropic material with penalization (SIMP) interpolation scheme to penalize intermediate densities and push the density design variables toward zero and one to achieve designs with distinct void and solid regions. The penalized densities are defined accordingly as, $E_\ell = \varepsilon + (1-\varepsilon) y_\ell^p$, $\ell = 1, \ldots, N$, where $p > 1$ is the SIMP penalty parameter and ε is a small positive number representing an Ersatz stiffness that prevents ill-conditioning of the problem in the low density regions in the design [28,29]. Variables, $\mathbf{y}$ and $\mathbf{E}$, will be used to compute the composite volume and stiffness, respectively, during the optimization iterations.

Second, to ensure that the orientation field is continuous, which facilitates the computation of curl constraints described in Section 5, the orientation design variables, $\hat{\theta} \in \left[-\frac{\pi}{2}, \frac{\pi}{2}\right]^M$, defined at the M CS-RBF support points, are mapped to $\theta \in \left[-\frac{\pi}{2}, \frac{\pi}{2}\right]^N$ at the N design points using a mapping matrix, $\hat{\boldsymbol{\Phi}}$, containing normalized CS-RBFs evaluated at the design points, i.e., $\theta = \hat{\boldsymbol{\Phi}}\hat{\theta}$. The $N \times M$ mapping matrix, $\hat{\boldsymbol{\Phi}}$, has components,

$$\hat{\phi}_{\ell q} = \hat{\phi}_q\left(\boldsymbol{x}_\ell\right) = \frac{\phi_q\left(\boldsymbol{x}_\ell\right)}{\sum_{s=1}^{M} \phi_s\left(\boldsymbol{x}_\ell\right)}, \tag{3}$$

where $\phi_q\left(\boldsymbol{x}_\ell\right)$ is Wendland's CS-RBF [30] evaluated at coordinate, $\boldsymbol{x}_\ell = \left(x_\ell, y_\ell\right)$, of design point ℓ. Wendland's CS-RBF takes the form,

$$\phi_q\left(\boldsymbol{x}_\ell\right) = (4r+1)\left[\max(0, 1-r)\right]^4, \quad q = 1, \ldots, M, \tag{4}$$

where $r = \left(1/r_s\right)\sqrt{(x_\ell - x_q)^2 + (y_\ell - y_q)^2 + \varrho^2}$, $\boldsymbol{x}_q = \left(x_q, y_q\right)$ is the coordinate of support point q, ϱ is a small positive number that prevents a divide by zero error in spatial derivatives of the CS-RBFs [31], and the support radius, r_s, defines the influence domain of the CS-RBF (see Fig. 1), beyond which CS-RBF takes zero value. The normalization of the CS-RBFs in (3) ensures that the bounds imposed on the orientation design variables, $\hat{\theta} \in [-\frac{\pi}{2}, \frac{\pi}{2}]^M$, at the support points are enforced on θ_ℓ, $\ell = 1, \ldots, N$, at the design points. Note that the orientation at any design point, ℓ, is always continuous due to the radially symmetric continuous CS-RBFs, that are centered at each of the M support points defined in the design domain. This continuity facilitates the sensitivity calculations required for gradient-based optimization. Previous studies indicate that the support point discretization can be much coarser than the design point discretization (i.e., M can be much smaller than N) to reduce computational cost with negligible influence on the optimized solution. Additionally, the support radius should be kept small to avoid restricting the orientation design space [7].

To fully define volume and stiffness properties of the composite, we use a projection method to generate fiber toolpaths from the orientation field, θ, in each optimization iteration. Similar projection methods have been used to generate spatially-varying lattices [16,17,32] or fiber toolpaths [4,5] from an orientation field in post-processing. Here, we adopt the approach recently taken by Ren et al. [15] and perform the

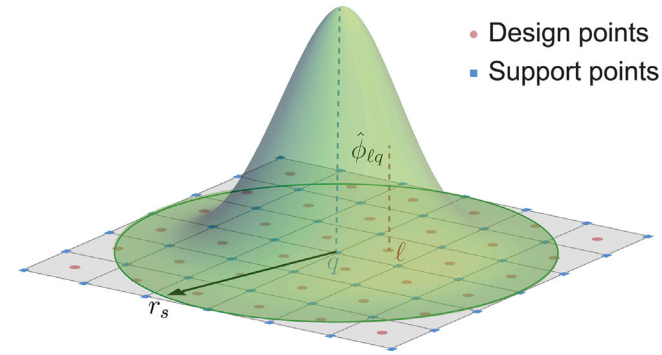

Fig. 1. Illustration of the mapping between quantities at the CS-RBF support points and the design points with CS-RBF support radius, r_s.

projection in each optimization iteration in order to more accurately account for the composite properties during design. The projection, described in detail in Section 3, leads to the material state field, $\hat{\chi} \in [0,1]^N$, where $\hat{\chi}_\ell = 0$ or $\hat{\chi}_\ell = 1$ indicates that matrix or fiber material properties, respectively, should be used at design point ℓ.

With $\mathbf{y}$ and $\hat{\chi}$, the composite volume, fiber volume, and matrix volume are computed as $v = \sum_{\ell=1}^{N} A_\ell y_\ell$, $v_f = \sum_{\ell=1}^{N} A_\ell y_\ell \hat{\chi}_\ell$, and $v_m = \sum_{\ell=1}^{N} A_\ell y_\ell \left(1 - \hat{\chi}_\ell\right)$, respectively. With $\mathbf{E}$ and $\hat{\chi}$, the global stiffness matrix, $\mathbf{K} = \sum_{\ell=1}^{N} E_\ell \mathbf{k}_\ell^0\left(z_\ell, \hat{\theta}\right)$, is assembled from the local element stiffness matrices,

$$\begin{aligned}(\mathbf{k}_\ell^0)_{jk} = {} & \hat{\chi}_\ell(z_\ell, \hat{\theta}) \int_{\Omega_\ell} \mathbf{B}_j{}^T \mathbf{D}_\ell^f\left(\theta_\ell\right) \mathbf{B}_k \, d\Omega_\ell \\ & + \left(1 - \hat{\chi}_\ell(z_\ell, \hat{\theta})\right) \int_{\Omega_\ell} \mathbf{B}_j{}^T \mathbf{D}^m \mathbf{B}_k \, d\Omega_\ell, \quad \ell = 1, \ldots, N\end{aligned} \tag{5}$$

(jk component shown), where Ω_ℓ is the domain of element ℓ, $\mathbf{B}$ is the strain–displacement matrix, $\mathbf{D}^m$ is the stiffness elasticity tensor (in matrix notation) of an isotropic material with Young's modulus, $\hat{E}_m$, and Poisson's ratio, ν_m, and $\mathbf{D}_\ell^f\left(\theta_\ell\right) = \mathbf{T}(\theta_\ell)\mathbf{Q}^f\mathbf{T}(\theta_\ell)^T$ is the stiffness elasticity tensor (in matrix notation) associated with the fiber material. The coordinate transformation matrix,

$$\mathbf{T}(\theta_\ell) = \begin{bmatrix} \cos^2(\theta_\ell) & \sin^2(\theta_\ell) & -2\sin(\theta_\ell)\cos(\theta_\ell) \\ \sin^2(\theta_\ell) & \cos^2(\theta_\ell) & 2\sin(\theta_\ell)\cos(\theta_\ell) \\ \sin(\theta_\ell)\cos(\theta_\ell) & -\sin(\theta_\ell)\cos(\theta_\ell) & \cos(2\theta_\ell) \end{bmatrix}, \tag{6}$$

is used to perform the fourth-order tensor transformation (in matrix notation) of the stiffness elasticity tensor,

$$\mathbf{Q}^f = \begin{bmatrix} Q_{11} & Q_{12} & 0 \\ Q_{12} & Q_{22} & 0 \\ 0 & 0 & Q_{66} \end{bmatrix}, \tag{7}$$

associated with fibers oriented at 0° from the horizontal. For an anisotropic fiber, the stiffness elasticity tensor, $\mathbf{Q}^f$, can be fully defined using the Young's modulus of the fiber material along the fiber direction (1-plane), $\hat{E}_{f1}$, the Young's modulus of the fiber material transverse to the fiber direction (2-plane), $\hat{E}_{f2}$, the shear modulus of the fiber material in the 1–2 plane, $\hat{G}_{12}$, and Poisson's ratio of the fiber material in the 1–2 plane, ν_{12}, such that [33],

$$Q_{11} = \frac{\hat{E}_{f1}}{1 - \nu_{12}\nu_{21}}, Q_{12} = \frac{\nu_{12}\hat{E}_{f2}}{1 - \nu_{12}\nu_{21}}, Q_{22} = \frac{\hat{E}_{f2}}{1 - \nu_{12}\nu_{21}}, Q_{66} = \hat{G}_{12}. \tag{8}$$

Note that since $\mathbf{D}_\ell^f\left(\theta_\ell\right)$ is a function of the orientation design variables, the portion of the element stiffness matrices associated with the fiber material in (5) must be updated in each optimization iteration. To increase computational efficiency, we adopt the approach proposed by Altassan et al. [34] and avoid the repeated numerical integrations needed to compute the first term in (5) in each iteration. Specifically,

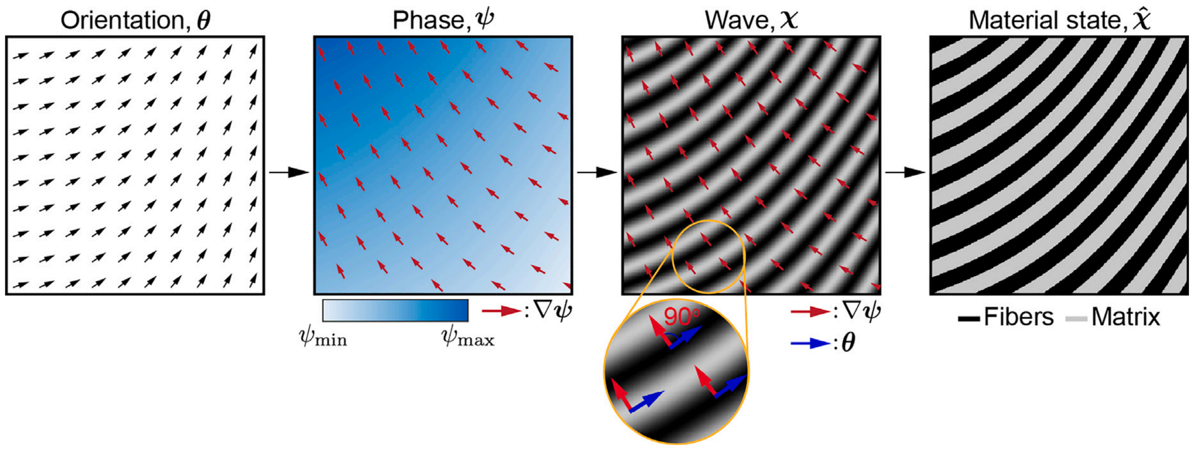

Fig. 2. Schematic of the transformation from orientation at the design points to fiber towpregs with distinct material states, where black represents fibers and gray represents matrix.

we use linear least squares regression to fit a Fourier series function, $\mathcal{F}(\theta)$, for each component of $\mathbf{D}^f(\theta) = \mathbf{T}(\theta)\mathbf{Q}^f\mathbf{T}(\theta)^T$, where

$$\mathcal{F}(\theta) = C_0 + C_1\cos(h\theta) + C_2\sin(h\theta) + C_3\cos(2h\theta) + C_4\sin(2h\theta), \tag{9}$$

$C_0, \ldots, C_4$ are the fitting function's coefficients, the sine and cosine functions are the fitting function's basis functions, $h = 2\pi/T$, and T is the periodicity of the fiber material. Note that the Fourier series fitting function used here can be expressed as $\mathcal{F}(\theta) = \sum_{s=0}^{4}[\mathbf{C}]_s c_s(\theta)$, where $[\mathbf{C}]_s$ is a matrix of the same size as $\mathbf{D}^f$ containing the coefficients of the sth terms of the Fourier series fitting functions and $c_s(\theta)$ is the basis function associated with the sth term. Then, the jk component of the element stiffness matrix in element ℓ can be rewritten as,

$$\begin{aligned}(\mathbf{k}^0_\ell)_{jk} &= \hat{\chi}_\ell(z_\ell,\hat{\boldsymbol{\theta}})\int_{\Omega_\ell}\mathbf{B}_j{}^T\mathcal{F}\left(\theta_\ell\right)\mathbf{B}_k\,d\Omega_\ell \\ &\quad+\left(1-\hat{\chi}_\ell(z_\ell,\hat{\boldsymbol{\theta}})\right)\int_{\Omega_\ell}\mathbf{B}_j{}^T\mathbf{D}^m\mathbf{B}_k\,d\Omega_\ell \\ &= \hat{\chi}_\ell(z_\ell,\hat{\boldsymbol{\theta}})\left[\sum_{s=0}^{4}\left[\int_{\Omega_\ell}\mathbf{B}_j{}^T[\mathbf{C}]_s\mathbf{B}_k\,d\Omega_\ell\right]c_s(\theta_\ell)\right] \\ &\quad+\left(1-\hat{\chi}_\ell(z_\ell,\hat{\boldsymbol{\theta}})\right)\int_{\Omega_\ell}\mathbf{B}_j{}^T\mathbf{D}^m\mathbf{B}_k\,d\Omega_\ell,\end{aligned} \tag{10}$$

where the two integrals in the second line of (10) are independent of the density and orientation design variables. These integrals are computed numerically during precomputations such that during the optimization iterations, we only need to compute the product of these precomputed integrals with the basis functions.

3. Obtaining the fiber–matrix distribution with finite length scale

To project the fiber orientation field, $\boldsymbol{\theta}$, to material state field, $\hat{\chi}$, as shown in Fig. 2, we adopt the analogy to wave theory first put forth by Rumpf and Pazos [32] for generating spatially-varying lattices.

We wish to generate a spatially-varying 2D wave with peaks of magnitude 1 indicating contours of the centerlines of the fiber material and troughs of magnitude 0 indicating contours of the centerlines of matrix material. A snapshot at time zero of such a wave that oscillates around a magnitude of 1/2 and with peak-to-peak amplitude of 1, can be expressed as

$$\chi(\boldsymbol{x}) = \frac{1}{2} + \frac{1}{2}\cos\left(\frac{2\pi}{d}(\psi(\boldsymbol{x}))\right), \tag{11}$$

where $\psi(\boldsymbol{x})$ is the time-independent phase function and d is the wavelength. Contours of the wave's peaks and troughs should align with the direction of vectors in the fiber orientation field, $\boldsymbol{\theta}$, i.e., the direction of wave propagation should be locally orthogonal to $\boldsymbol{\theta}$ (see third column of Fig. 2). Mathematically, this condition states that the gradient of the phase function, $\nabla\psi(\boldsymbol{x})$, should be locally orthogonal to the continuous function, $\theta(\boldsymbol{x})$, to which the discrete scalar field, $\boldsymbol{\theta}$, belongs, i.e.,

$$\nabla\psi(\boldsymbol{x}) = \begin{bmatrix}-\sin\theta(\boldsymbol{x})\\ \cos\theta(\boldsymbol{x})\end{bmatrix}. \tag{12}$$

The differential equation in (12) can be used to solve for the phase function, $\psi(\boldsymbol{x})$, in (11). Note that for the simplest case of constant $\boldsymbol{\theta}$, (12) indicates that $\psi(\boldsymbol{x}) = k_x x + k_y y$, where $k_x = -\sin\theta$ and $k_y = \cos\theta$ are constants, and we arrive at the well-known expression, $\psi(\boldsymbol{x}) = \mathbf{k}\cdot\boldsymbol{x}$, of wave theory. In our case, in which we have non-constant $\boldsymbol{\theta}$, we use the finite difference method to approximate the solution, $\psi(\boldsymbol{x})$, to (12).

Before approximating the solution to (12), we introduce discrete representations of the wave and phase functions, $\chi(\mathbf{z},\hat{\boldsymbol{\theta}})$ and $\boldsymbol{\psi}(\mathbf{z},\hat{\boldsymbol{\theta}})$, respectively, both of which have length N. The discrete wave and phase functions depend on the spatial coordinate, $\boldsymbol{x}$, through the values of the design variables stored in $\mathbf{z}$ and $\hat{\boldsymbol{\theta}}$. Additionally, we introduce a vector of spatial weighting factors, $\boldsymbol{\alpha}(\mathbf{z}) \in [0,1]^N$, which allows for degraded accuracy of the phase function approximation in regions where composite material does not exist (i.e., for all ℓ in which the density design variable, z_ℓ, approaches zero) and, as a result, improves alignment of the wave function with the orientation field in regions where composite material does exist [17]. Then, we can write the gradient of the discrete phase function as

$$\nabla\psi_\ell(z_\ell,\theta_\ell) = \begin{bmatrix}-\alpha_\ell\sin\theta_\ell\\ \alpha_\ell\cos\theta_\ell\end{bmatrix}, \tag{13}$$

for $\ell = 1,\ldots,N$, where α_ℓ is defined through a Heaviside projection, i.e.,

$$\alpha_\ell(z_\ell) = \frac{\tanh(\beta\eta_\alpha) + \tanh\beta(z_\ell - \eta_\alpha)}{\tanh(\beta\eta_\alpha) + \tanh\beta(1-\eta_\alpha)}, \tag{14}$$

for $\ell = 1,\ldots,N$, such that α_ℓ is pushed to 0 or 1 when z_ℓ falls below or above, respectively, a threshold value, η_α. In (14), β, dictates steepness of the Heaviside function.

According to the finite difference method, $\nabla\boldsymbol{\psi}(\mathbf{z},\hat{\boldsymbol{\theta}}) \approx \mathbf{A}\boldsymbol{\psi}(\mathbf{z},\hat{\boldsymbol{\theta}})$, where $\mathbf{A}$ is the centered finite difference matrix. Then the discretized phase function can be approximated as

$$\boldsymbol{\psi}(\mathbf{z},\hat{\boldsymbol{\theta}}) = \left((\mathbf{A}^T\mathbf{A})^{-1}\mathbf{A}^T\right)\nabla\boldsymbol{\psi}(\mathbf{z},\hat{\boldsymbol{\theta}}) \tag{15}$$

according to the least-squares method [35]. With an approximation of the discretized phase function, $\boldsymbol{\psi}(\mathbf{z},\hat{\boldsymbol{\theta}})$, the discretized wave function can be written as

$$\chi(\mathbf{z},\hat{\boldsymbol{\theta}}) = \frac{1}{2} + \frac{1}{2}\cos\left(\frac{2\pi}{d}(\boldsymbol{\psi}(\mathbf{z},\hat{\boldsymbol{\theta}}) - \psi_0)\right), \tag{16}$$

where ψ_0 is the value of the phase function at an anchor location, which is introduced to fix the initial position of the wave function and improve convergence of the optimization problem [15]. We apply another Heaviside projection to the discretized wave function, $\chi(\mathbf{z}, \hat{\boldsymbol{\theta}})$, to arrive at $\hat{\chi}(\mathbf{z}, \hat{\boldsymbol{\theta}})$, which contains distinct material states of 0 or 1 that indicate matrix material or fiber material, respectively, at each design point (see fourth column of Fig. 2), i.e.,

$$\hat{\chi}_\ell(z_\ell, \hat{\theta}_\ell) = \frac{\tanh(\beta\eta) + \tanh\beta(\chi_\ell(z_\ell, \hat{\theta}_\ell) - \eta)}{\tanh(\beta\eta) + \tanh\beta(1-\eta)}, \tag{17}$$

where η and β are the Heaviside threshold and steepness parameters, respectively.

It is noted that the design variables, $\hat{\boldsymbol{\theta}}$, are transformed in four steps to the final material state, $\hat{\chi}$, (see second to fourth columns of Fig. 2) as compared to the formulation proposed by Ren et al. [15], where the gradients of the discrete phase function, $\nabla\boldsymbol{\psi}$, are used as the design variables and the transformation from the design variables to the final material state is performed in three steps. In the work by Ren et al. [15], an additional step is required to calculate the discrete orientation field at the design points for the assembly of the local stiffness matrix. As shown in Section 5, the CS-RBF mapping described in Section 2, ensures the C^1 continuity of the orientation field at the design points, which allows us to obtain an analytical expression of the curl constraints. As a result, we avoid expensive finite difference calculations in approximating the spatial derivative of a discrete fiber orientation vector field needed to obtain the local curl values. Additionally, the approach pursued here, which relies on an analogy to wave theory, only performs well for a smoothly-varying orientation field [16,17]. When used as a post-processing step, many strategies have been proposed to obtain smoothly-varying fiber orientations before the phase calculation [17,36–39]. Here, the CS-RBF mapping ensures continuity and smoothness of the mapped orientation at the design points, and thus, eliminates the need for additional steps to smooth the orientation field.

4. Controlling physical properties of the fiber–matrix distribution

Towpregs, sometimes referred to as prepregs, are continuous fiber tows impregnated with polymeric matrix material. They are most commonly used in AFP processes, but there are also MEX processes that use towpregs directly as feedstock (e.g., towpreg co-extrusion and towpreg extrusion). Towpregs in this work consist of a fiber tow sandwiched between matrix material.

We can use various parameters of the wave projection method discussed in Section 3 to control physical properties of the fiber towpregs. The wavelength, d, in (16) controls the spacing between peaks and troughs of the wave field, χ, and ultimately the center-to-center distance between either fibers or matrix in the material state field, $\hat{\chi}$. The center-to-center distance in $\hat{\chi}$ represents the width of a fiber towpreg (see light orange regions in Fig. 3). As we increase d from 0.1 mm to 0.5 mm in Fig. 3, we observe that the fiber towpreg width after the Heaviside projection corresponds to 0.1 mm (top row of Fig. 3) and 0.5 mm (bottom row of Fig. 3), respectively. In (17), η controls the threshold position of the Heaviside projection operator and allows us to control the total fiber width within a fiber towpreg. With a fixed d, i.e., a fixed fiber towpreg width, an increasing value of η narrows the width of the fiber (indicated by black) and increases the amount of matrix material (indicated by gray) within the fiber towpreg (see second to fourth columns of Fig. 3). The above discussion is relevant to the ideal case shown in Fig. 3, where no towpreg curvature is present and the per towpreg matrix and fiber volume fractions are exactly $v_{m,\text{tow}} = \eta$ and $v_{f,\text{tow}} = 1 - \eta$, respectively. However, since curvature causes variations in the towpreg and fiber widths along the length of a towpreg, the above expressions for $v_{m,\text{tow}}$ and $v_{f,\text{tow}}$ are not exact, but close approximations (this point is illustrated with an example in Section 8.2.2). Nevertheless, together d and η provide control over fiber towpreg width and fiber volume fraction within a towpreg such that we can tailor designs for specific CFRP manufacturing technologies.

5. Description of local curl constraints on fiber orientation

It has been shown that local fiber tow curvature, $\kappa(\boldsymbol{x})$, in CFRPs can be effectively controlled by restricting the out-of-plane component of the curl, $\zeta(\boldsymbol{x})$, of a vector field of fiber orientations [7,23,40,41]. We refer the reader to the author's previous work [7] for a detailed discussion on the relationship between curl and curvature, and here, only highlight the key equations needed to arrive at expressions for the local curl, $\zeta_\ell(\boldsymbol{\theta})$, at design points $\ell = 1, \ldots, N$, needed in the curl constraint functions appearing in (1). First, we assume a spatial distribution of fiber orientations, $\theta(\boldsymbol{x})$, and let $\mathbf{v}(\boldsymbol{x}) = \cos(\theta(\boldsymbol{x}))\hat{\mathbf{i}} + \sin(\theta(\boldsymbol{x}))\hat{\mathbf{j}}$ be the associated orientation vector field, where $\hat{\mathbf{i}}$ and $\hat{\mathbf{j}}$ are unit vectors of the in-plane x and y coordinate axes, respectively. Although curl is a vector quantity, the only non-zero component of the curl is the out-of-plane component (i.e., in the $\hat{\mathbf{k}}$ direction) for the 2D fiber orientation fields considered here. To simplify terminology in the following, we refer to the out-of-plane component of the curl of $\mathbf{v}(\boldsymbol{x})$,

$$\begin{aligned}\zeta(\boldsymbol{x}) &= (\nabla \times \mathbf{v}(\boldsymbol{x})) \cdot \hat{\mathbf{k}} \\ &= \frac{\partial\theta(\boldsymbol{x})}{\partial x}\cos\theta(\boldsymbol{x}) + \frac{\partial\theta(\boldsymbol{x})}{\partial y}\sin\theta(\boldsymbol{x}) \\ &= \nabla\theta(\boldsymbol{x}) \cdot \mathbf{v}(\boldsymbol{x}),\end{aligned} \tag{18}$$

simply as curl of $\mathbf{v}(\boldsymbol{x})$. Next, we recall that the curvature of a fiber tow can be expressed mathematically as the magnitude of the derivative of its unit tangent vector, such that $\kappa(\boldsymbol{x}) = \frac{\partial\theta(\boldsymbol{x})}{\partial x}\cos\theta(\boldsymbol{x}) + \frac{\partial\theta(\boldsymbol{x})}{\partial y}\sin\theta(\boldsymbol{x})$. Note that while (18) indicates equivalence between the curvature of a fiber tow, $\kappa(\boldsymbol{x})$, and the curl, $\zeta(\boldsymbol{x})$, of the underlying 2D vector field, the quantities will only be approximately equal in practice, i.e. $\kappa(\boldsymbol{x}) \approx \zeta(\boldsymbol{x})$, since the curvature of toolpaths generated using the wave projection method described in Section 3 may not align precisely with the underlying orientation field. Nevertheless, the curl of $\mathbf{v}(\boldsymbol{x})$ will have a direct influence on the curvature of the fiber tows generated from $\mathbf{v}(\boldsymbol{x})$ and can be used to constrain the local curvature of fiber tows. Using the definition of curl in (18) and the fiber orientation design variables, $\hat{\boldsymbol{\theta}}$, defined using CS-RBFs in (3), we arrive at the expression for curl at design point ℓ,

$$\zeta_\ell(\boldsymbol{x}_\ell) = \cos\theta_\ell\left(\sum_{q=1}^{M}\hat{\phi}_{q,x}(\boldsymbol{x}_\ell)\,\hat{\theta}_q\right) + \sin\theta_\ell\left(\sum_{q=1}^{M}\hat{\phi}_{q,y}(\boldsymbol{x}_\ell)\,\hat{\theta}_q\right), \tag{19}$$

where $\boldsymbol{x}_\ell = (x_\ell, y_\ell)$ are the coordinates of design point ℓ. Note that the local curl defined in (19) lies on a C^1 continuous function due to the mapping of fiber orientations at each design point from those at support points of continuous CS-RBFs. The partial derivatives $\hat{\phi}_{q,x} = \partial\hat{\phi}_q/\partial x$ can be collected into an $N \times M$ matrix, $\hat{\boldsymbol{\Phi}}_{,x}$, with components,

$$\hat{\phi}_{\ell q,x} = \hat{\phi}_{q,x}(\boldsymbol{x}_\ell) = \frac{\phi_{q,x}(\boldsymbol{x}_\ell)\sum_{s=1}^{M}\phi_s(\boldsymbol{x}_\ell) - \phi_q(\boldsymbol{x}_\ell)\sum_{s=1}^{M}\phi_{s,x}(\boldsymbol{x}_\ell)}{\left[\sum_{s=1}^{M}\phi_s(\boldsymbol{x}_\ell)\right]^2}, \tag{20}$$

where $\phi_{q,x}(\boldsymbol{x}_\ell) = (-20)\dfrac{x_\ell - x_q}{r_s^{\,2}}\left[\max(0, 1-r)\right]^3.$

The partial derivatives $\hat{\phi}_{q,y} = \partial\hat{\phi}_q/\partial y$ can also be collected into an $N \times M$ matrix, $\hat{\boldsymbol{\Phi}}_{,y}$, with components,

$$\hat{\phi}_{\ell q,y} = \hat{\phi}_{q,y}(\boldsymbol{x}_\ell) = \frac{\phi_{q,y}(\boldsymbol{x}_\ell)\sum_{s=1}^{M}\phi_s(\boldsymbol{x}_\ell) - \phi_q(\boldsymbol{x}_\ell)\sum_{s=1}^{M}\phi_{s,y}(\boldsymbol{x}_\ell)}{\left[\sum_{s=1}^{M}\phi_s(\boldsymbol{x}_\ell)\right]^2}, \tag{21}$$

where $\phi_{q,y}(\boldsymbol{x}_\ell) = (-20)\dfrac{y_\ell - y_q}{r_s^{\,2}}\left[\max(0, 1-r)\right]^3.$

In (20) and (21), (x_q, y_q) are the coordinates of support point q.

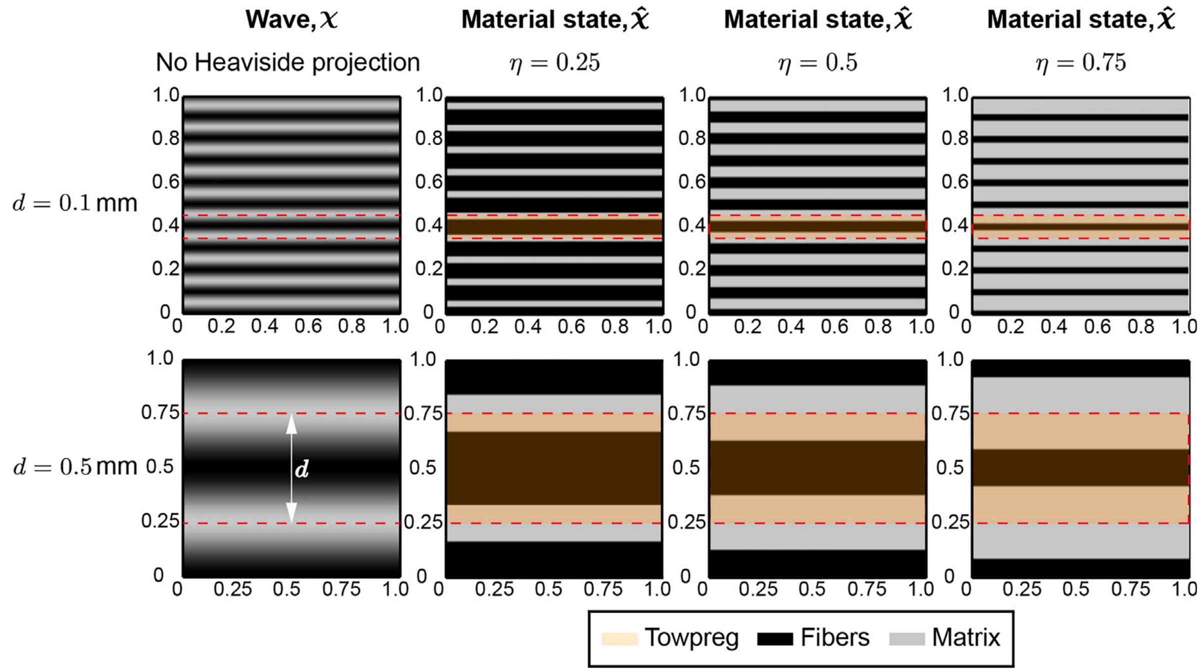

Fig. 3. Illustration of how fiber towpreg width and fiber volume fraction within a fiber towpreg can be controlled by parameters of the wave projection method. The wavelength, d, controls the fiber towpreg width ($d = 0.1$ mm in the top row and $d = 0.5$ mm in the bottom row). As the Heaviside projection threshold, η, increases from left to right, the fiber volume fraction within the fiber towpreg decreases. Units are in mm.

6. Augmented Lagrangian solution scheme

The problem formulation in (1) contains a large number of local curl constraints, i.e., one for each design point in the domain. To handle these many local constraints, we adopt the augmented Lagrangian (AL) solution scheme, which is expected to obtain the solution of the original constrained problem by solving a series of unconstrained problems [24,25]. Here, we use a modified version of the AL method proposed by Senhora et al. [42] where the unconstrained sub-problem at the kth step of the AL method is stated as

$$\min_{\substack{\mathbf{z}^{(k)} \in [0,1]^N \\ \hat{\boldsymbol{\theta}}^{(k)} \in \left[-\frac{\pi}{2}, \frac{\pi}{2}\right]^M}} L(\mathbf{z}^{(k)}, \hat{\boldsymbol{\theta}}^{(k)}) = f(\mathbf{z}^{(k)}, \hat{\boldsymbol{\theta}}^{(k)}) + J(\mathbf{z}^{(k)}, \hat{\boldsymbol{\theta}}^{(k)}). \tag{22}$$

In (22), $L(\mathbf{z}^{(k)}, \hat{\boldsymbol{\theta}}^{(k)})$ is the AL function, $f(\mathbf{z}^{(k)}, \hat{\boldsymbol{\theta}}^{(k)})$ is the objective function of the original constrained problem,

$$J(\mathbf{z}^{(k)}, \hat{\boldsymbol{\theta}}^{(k)}) = \sum_{j=1}^{2} \left[\lambda_j^{(k)} h_j(\mathbf{z}^{(k)}, \hat{\boldsymbol{\theta}}^{(k)}) + \frac{\mu^{(k)}}{2} h_j(\mathbf{z}^{(k)}, \hat{\boldsymbol{\theta}}^{(k)})^2\right] + \frac{1}{N} \sum_{j=3}^{N_c} \left[\lambda_j^{(k)} h_j(\mathbf{z}^{(k)}, \hat{\boldsymbol{\theta}}^{(k)}) + \frac{\mu^{(k)}}{2} h_j(\mathbf{z}^{(k)}, \hat{\boldsymbol{\theta}}^{(k)})^2\right] \tag{23}$$

is the penalty function,

$$h_j(\mathbf{z}^{(k)}, \hat{\boldsymbol{\theta}}^{(k)}) = \max\left[g_j(\mathbf{z}^{(k)}, \hat{\boldsymbol{\theta}}^{(k)}), -\frac{\lambda_j^{(k)}}{\mu^{(k)}}\right], \quad j = 1, \ldots, N_c \tag{24}$$

are equality constraints determined from the original $N_c = N + 2$ inequality constraints using slack variables (see, for example, [24,25, 42]), and

$$\mathbf{g}(\mathbf{z}^{(k)}, \hat{\boldsymbol{\theta}}^{(k)}) = \left[{}^{v}g(\mathbf{z}), {}^{vf}g(\mathbf{z}, \hat{\boldsymbol{\theta}}), {}^{\zeta}g_1(\hat{\boldsymbol{\theta}}), \ldots, {}^{\zeta}g_N(\hat{\boldsymbol{\theta}})\right] \tag{25}$$

holds the N_c inequality constraints of the constrained problem in (1). Similar to the quadratic penalty method, the quadratic terms of $J(\mathbf{z}^{(k)}, \hat{\boldsymbol{\theta}}^{(k)})$ impose severe penalization to constraint violations as the AL penalty factor, $\mu^{(k)}$, increases [24,25]. The terms of $J(\mathbf{z}^{(k)}, \hat{\boldsymbol{\theta}}^{(k)})$ that are linear in the constraints contain a Lagrange multiplier estimator, $\lambda_j^{(k)}$, for each constraint, $h_j(\mathbf{z}^{(k)}, \hat{\boldsymbol{\theta}}^{(k)})$, $j = 1, \ldots, N_c$, and were introduced in the AL method to reduce ill-conditioning of the quadratic penalty method (note that the Lagrangian of the original constrained problem is the sum of the objective function and the linear terms of the penalty function). To ensure the objective function and penalty term are of a similar order of magnitude and that the magnitude of the penalty term is independent of the number of local constraints, we impose the scale factor, $1/N$, proposed by Senhora et al. [42] on the portion of the penalty term, $J(\mathbf{z}^{(k)}, \hat{\boldsymbol{\theta}}^{(k)})$, associated with the local constraints.

The quadratic penalty factor and Lagrange multiplier estimators are updated after every kth subproblem according to

$$\mu^{(k+1)} = \min\left[\xi \mu^{(k)}, \mu_{\max}\right] \tag{26}$$

and

$$\lambda_j^{(k+1)} = \lambda_j^{(k)} + \mu^{(k)} h_j(\mathbf{z}^{(k)}, \boldsymbol{\theta}^{(k)}), \; j = 1, \ldots, N_c, \tag{27}$$

respectively, where $\xi > 1$ is a constant AL penalty update factor. Gradually increasing the quadratic penalty factor over the subproblems to an upper limit, $\mu_{\max}$, as described in (26), reduces the possibility of ill-conditioning or other numerical instabilities [43]. In (27), the Lagrange multiplier estimators are updated based on the first order optimality conditions of the original constrained problem in (1) and the unconstrained subproblem. The performance of the AL method is influenced by the initial penalty coefficient, $\mu^{(0)}$, maximum penalty coefficient, $\mu_{\max}$, penalty update factor, ξ, and initial Lagrange multiplier estimators, $\lambda^{(0)}$. The parameters are known to be problem-dependent and may require empirical adjustment. It is noted that the AL solution scheme is adopted to handle local constraints rather than aggregating them into a single global constraint or several clustered constraints. In prior work, we show that this local approach promotes convergence of the optimization problem and ensures that the curl constraints are satisfied at every design point [7].

The AL algorithm considered here is illustrated in Fig. 4. It consists of an inner loop in which the design variables are updated for a small number of iterations, `MMAIter`, using the method of moving

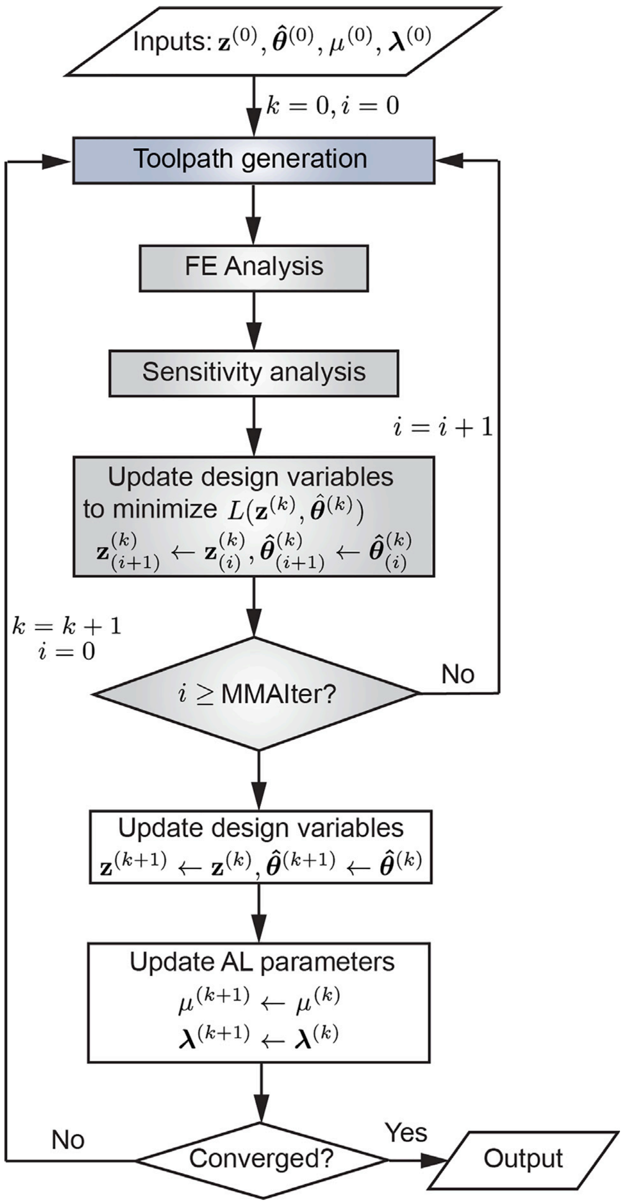

Fig. 4. Flowchart of the topology optimization algorithm with AL as the solution scheme for compliance minimization of CFRPs with integrated fiber toolpaths generation, with global volume constraints, fiber volume constraints, and local curl constraints.

asymptotes (MMA) [44] to reduce the value of the AL function, and an outer loop in which the AL parameters are updated. A key novelty of the algorithm shown in Fig. 4 is the introduction of a toolpath generation step each time the design variables are updated (in either the inner or outer loop). This toolpath generation step ensures that the mechanical properties of the CRFP structure fed to the finite element analysis are more representative of the manufactured structure. The algorithm is considered to have converged when either a prescribed maximum number of iterations is reached or when the change in design variables is small, i.e., when

$$\begin{aligned} &\frac{1}{N}\sum_{\ell=1}^{N}\left(\left(z_\ell\right)^{(k)}_{(i+1)} - \left(z_\ell\right)^{(k)}_{(i)}\right) < \texttt{tolD} \text{ and} \\ &\frac{1}{N}\sum_{\ell=1}^{N}\left(\left(\hat{\theta}_q\right)^{(k)}_{(i+1)} - \left(\hat{\theta}_q\right)^{(k)}_{(i)}\right) < \texttt{tolD}, \end{aligned} \tag{28}$$

and when the curl constraints are close to their allowable limits, i.e., when

$$\max\{\zeta_1/\zeta_{\text{all}}, \ldots, \zeta_N/\zeta_{\text{all}}\} < \texttt{tolC}. \tag{29}$$

In (28) and (29), tolD and tolC are prescribed tolerance values on the design variable convergence and curl constraint convergence, respectively. In (28), $\left(z_\ell\right)^{(k)}_{(i+1)}$ and $\left(z_\ell\right)^{(k)}_{(i)}$ are the density design variable at design point ℓ at two consecutive inner loop iterations of the kth AL sub-problem and $(\hat{\theta}_\ell)^{(k)}_{(i+1)}$ and $(\hat{\theta}_\ell)^{(k)}_{(i)}$ are the orientation design variable at design point ℓ at two consecutive inner loop iterations of the kth AL sub-problem.

7. Sensitivity analysis

The modified AL function, $L(\mathbf{z}^{(k)}, \hat{\boldsymbol{\theta}}^{(k)})$, in (22) is minimized using gradient-based optimization, which requires its first derivatives with respect to the design variables. In this section, no summation is assumed on repeated indices. For simplicity of notation, we drop the superscript, k, and write the derivative as

$$\begin{aligned} \frac{\partial L}{\partial \mathbf{W}} &= \frac{\partial f}{\partial \mathbf{W}} + \frac{\partial J}{\partial \mathbf{W}} \\ &= \frac{\partial f}{\partial \mathbf{W}} + \sum_{j=1}^{2}\left[\lambda_j + \mu h_j(\mathbf{z}, \hat{\boldsymbol{\theta}})\right]\frac{\partial h_j}{\partial \mathbf{W}} + \frac{1}{N}\sum_{j=3}^{N_c}\left[\lambda_j + \mu h_j(\mathbf{z}, \hat{\boldsymbol{\theta}})\right]\frac{\partial h_j}{\partial \mathbf{W}}, \end{aligned} \tag{30}$$

where $\mathbf{W} = [\mathbf{z}, \hat{\boldsymbol{\theta}}]$, $\partial f/\partial \mathbf{W} = [\partial f/\partial \mathbf{z}, \partial f/\partial \hat{\boldsymbol{\theta}}]$, and $\partial h_j/\partial \mathbf{W} = [\partial h_j/\partial \mathbf{z}, \partial h_j/\partial \hat{\boldsymbol{\theta}}]$. Thus, to compute $\partial L/\partial \mathbf{W}$, we need derivatives of the objective and constraint functions with respect to the design variables.

The derivatives of the objective function with respect to the density design variables are computed as,

$$\frac{\partial f}{\partial \mathbf{z}} = -\mathbf{u}^T\frac{\partial \mathbf{K}}{\partial \mathbf{z}}\mathbf{u}, \tag{31}$$

where

$$\frac{\partial \mathbf{k}_k}{\partial z_\ell} = \begin{cases} \dfrac{\partial y_\ell}{\partial z_\ell}\dfrac{\partial E_\ell}{\partial y_\ell}\mathbf{k}^0_\ell\left(z_\ell, \theta_\ell\right) + E_\ell\dfrac{\partial \hat{\chi}_\ell}{\partial z_\ell}(\mathbf{k}^f_\ell\left(\theta_\ell\right) - \mathbf{k}^m_\ell) & \text{if } k = \ell \\ 0 & \text{otherwise.} \end{cases} \tag{32}$$

In (32), $(\mathbf{k}^f_\ell)_{jk}\left(\theta_\ell\right) = \sum_{s=0}^{n}\left[\int_{\Omega_\ell}\mathbf{B}_j^T[\mathbf{C}]_s\mathbf{B}_k d\Omega_\ell\right]c_s(\theta_\ell)$, $(\mathbf{k}^m_\ell)_{jk} = \int_{\Omega_\ell}\mathbf{B}_j^T\mathbf{D}^m\mathbf{B}_k d\Omega_\ell$, $\partial \mathbf{y}/\partial \mathbf{z} = \mathbf{P}^T$,

$$\frac{\partial E_k}{\partial y_\ell} = \begin{cases} p(1-\varepsilon){y_\ell}^{p-1} & \text{if } k = \ell \\ 0 & \text{otherwise,} \end{cases} \tag{33}$$

and

$$\frac{\partial \hat{\chi}_k}{\partial z_\ell} = \begin{cases} \dfrac{\partial \hat{\chi}_\ell}{\partial \chi_\ell}\dfrac{\partial \chi_\ell}{\partial \psi_\ell}\dfrac{\partial \psi_\ell}{\partial \nabla\psi_\ell}\dfrac{\partial \nabla\psi_\ell}{\partial \alpha_\ell}\dfrac{\partial \alpha_\ell}{\partial z_\ell} & \text{if } k = \ell \\ 0 & \text{otherwise.} \end{cases} \tag{34}$$

The derivatives used in the chain rule for the derivative of the material state with respect to the density design variables in (34) are,

$$\frac{\partial \hat{\chi}_\ell}{\partial \chi_\ell} = \beta\left(\frac{1 - \tanh^2(\beta(\chi_\ell - \eta))}{\tanh(\beta\eta) + \tanh(\beta(1-\eta))}\right), \tag{35}$$

$$\frac{\partial \chi_\ell}{\partial \psi_\ell} = -\frac{\pi}{d}\sin\left(\frac{2\pi}{d}(\psi_\ell - \psi_0)\right), \tag{36}$$

$$\frac{\partial \psi_\ell}{\partial \nabla\psi_\ell} = \left(\mathbf{A}^T\mathbf{A}\right)^{-1}\mathbf{A}^T, \tag{37}$$

$$\frac{\partial \nabla\psi_\ell}{\partial \alpha_\ell} = \begin{bmatrix} -\sin\theta_\ell \\ \cos\theta_\ell \end{bmatrix}, \tag{38}$$

and,

$$\frac{\partial \alpha_\ell}{\partial z_\ell} = \beta\left(\frac{1 - \tanh^2(\beta(z_\ell - \eta_\alpha))}{\tanh(\beta\eta_\alpha) + \tanh(\beta(1-\eta_\alpha))}\right). \tag{39}$$

The derivatives of the objective function with respect to the orientation design variables are computed using the chain rule, i.e.,

$$\frac{\partial f}{\partial \hat{\theta}} = \frac{\partial \theta}{\partial \hat{\theta}} \frac{\partial f}{\partial \theta}, \tag{40}$$

where $\partial \theta / \partial \hat{\theta} = \hat{\boldsymbol{\Phi}}^T$,

$$\frac{\partial f}{\partial \theta} = -\mathbf{u}^T \frac{\partial \mathbf{K}}{\partial \theta} \mathbf{u}, \tag{41}$$

$$\frac{\partial \mathbf{k}_k}{\partial \theta_\ell} = E_k \frac{\partial \mathbf{k}_k^0}{\partial \theta_\ell}, \tag{42}$$

$$\frac{\partial \left(\mathbf{k}_k^0\right)_{mn}}{\partial \theta_\ell} = \begin{cases} \dfrac{\partial \hat{\chi}_\ell}{\partial \theta_\ell} (\mathbf{k}_\ell^f\left(\theta_\ell\right) - \mathbf{k}_\ell^m) + \hat{\chi}_\ell \left[\displaystyle\sum_{s=0}^{n} \left[\int_{\Omega_\ell} \mathbf{B}_j{}^T [\mathbf{C}]_s \mathbf{B}_k \, d\Omega_\ell \right] \dfrac{\partial c_s(\theta_\ell)}{\partial \theta_\ell} \right] & \text{if } k = \ell \\ 0 & \text{otherwise}, \end{cases} \tag{43}$$

$\partial c_s\left(\theta_\ell\right)/\partial \theta_\ell$, $s = 0, \dots, n$ are the derivatives of the basis functions in (9), and

$$\frac{\partial \hat{\chi}_k}{\partial \theta_\ell} = \begin{cases} \dfrac{\partial \hat{\chi}_\ell}{\partial \chi_\ell} \dfrac{\partial \chi_\ell}{\partial \psi_\ell} \dfrac{\partial \psi_\ell}{\partial \nabla \psi_\ell} \dfrac{\partial \nabla \psi_\ell}{\partial \theta_\ell} & \text{if } k = \ell \\ 0 & \text{otherwise}. \end{cases} \tag{44}$$

The only derivative used in the chain rule for the derivative of the material state with respect to the orientation field in (44) that has not been defined is

$$\frac{\partial \nabla \psi_\ell}{\partial \theta_\ell} = -\begin{bmatrix} \alpha_\ell \cos \theta_\ell \\ \alpha_\ell \sin \theta_\ell \end{bmatrix}. \tag{45}$$

The derivatives of the constraints, in the form of the equality constraints used in the AL method, are

$$\frac{\partial h_j}{\partial \mathbf{W}} = \begin{cases} \dfrac{\partial g_j}{\partial \mathbf{W}} & \text{if } g_j > -\dfrac{\lambda_j}{\mu} \\ 0 & \text{otherwise} \end{cases} \tag{46}$$

for $j = 1, \dots, N_c$, where $\partial g_j/\partial \mathbf{W} = [\partial g_j/\partial \mathbf{z}, \partial g_j/\partial \hat{\theta}]$ and the derivative in (46) is continuous since λ_j and μ remain constant in the kth AL step. The global composite volume constraint, ${}^{v}g$, is a function of only $\mathbf{z}$, i.e., $\partial ({}^{v}g)/\partial \hat{\theta} = \mathbf{0}$, and thus, we only need the derivative of ${}^{v}g$ with respect to the density design variables, which is computed using the chain rule, i.e.,

$$\frac{\partial ({}^{v}g)}{\partial \mathbf{z}} = \frac{\partial \mathbf{y}}{\partial \mathbf{z}} \frac{\partial ({}^{v}g)}{\partial \mathbf{y}}, \quad \text{where} \quad \frac{\partial ({}^{v}g)}{\partial \mathrm{y}_\ell} = \frac{A_\ell}{\sum_{k=1}^{N} A_k}. \tag{47}$$

The global fiber volume constraint, ${}^{vf}g$, which limits the total volume fraction of fiber in the design domain, is a function of both $\mathbf{z}$ and $\hat{\theta}$, and thus, we need the derivative of ${}^{vf}g$ with respect to the density and the orientation design variables, which are computed using the chain rule, i.e.,

$$\frac{\partial \left({}^{vf}g\right)}{\partial z_\ell} = \frac{A_\ell}{\sum_{k=1}^{N} A_k} \left(\hat{\chi}_\ell \frac{\partial y_\ell}{\partial z_\ell} + y_\ell \frac{\partial \hat{\chi}_\ell}{\partial z_\ell} \right) \tag{48}$$

and

$$\frac{\partial \left({}^{vf}g\right)}{\partial \hat{\theta}} = \frac{\partial \theta}{\partial \hat{\theta}} \frac{\partial \left({}^{vf}g\right)}{\partial \theta}, \tag{49}$$

where

$$\frac{\partial \left({}^{vf}g\right)}{\partial \theta_\ell} = \frac{A_\ell y_\ell}{\sum_{k=1}^{N} A_k} \frac{\partial \hat{\chi}_\ell}{\partial \theta_\ell}. \tag{50}$$

Lastly, the local curl constraints are functions of only $\hat{\theta}$, i.e., $\partial \left({}^{\zeta}g_\ell\right)/\partial \mathbf{z} = \mathbf{0}$, $\ell = 1, \dots, N$, so we only need to calculate the derivatives with respect to $\hat{\theta}$, which are,

$$\frac{\partial \left({}^{\zeta}g_\ell\right)}{\partial \hat{\theta}_q} = 2\zeta_\ell \frac{\partial \zeta_\ell}{\partial \hat{\theta}_q}, \quad \ell = 1, \dots, N \tag{51}$$

where

$$\begin{aligned} \frac{\partial \zeta_\ell}{\partial \hat{\theta}_q} = {} & \hat{\phi}_{\ell q,x} \cos(\theta_\ell) - \hat{\phi}_{\ell q} \sin(\theta_\ell) \sum_{q=1}^{M} \hat{\phi}_{q,x}(\hat{\theta}_q) + \hat{\phi}_{\ell q,y} \sin(\theta_\ell) \\ & + \hat{\phi}_{\ell q} \cos(\theta_\ell) \sum_{q=1}^{M} \hat{\phi}_{q,y}(\hat{\theta}_q). \end{aligned} \tag{52}$$

In (52), $\hat{\phi}_{\ell q}, \hat{\phi}_{\ell q,x}, \hat{\phi}_{\ell q,y}$ are components of the $\hat{\boldsymbol{\Phi}}, \hat{\boldsymbol{\Phi}}_{,x}, \hat{\boldsymbol{\Phi}}_{,y}$ matrices, respectively, for design point ℓ and support point q.

8. Numerical examples

We present four numerical examples to demonstrate the key features of the proposed formulation for toolpath-integrated topology optimization of maximally-stiff CFRPs with constraints on structure volume, fiber volume, and curvature of fiber toolpaths. The optimization parameters considered for each example are provided in Table 1. All examples are discretized using quadrilateral finite elements and run on a laptop with an Intel Core i7 processor, 2.1 GHz, 32 GB RAM, and MATLAB R2022b.

8.1. Navigating prescribed voids with high curvatures

In this section, we design the four cantilever beams with domain and boundary conditions shown in Fig. 5, three of which have prescribed voids. This example was considered by Ren et al. [15] to illustrate toolpath-integrated topology optimization of CFRPs. While not a direct comparison with the results of Ren et al. [15] due to differences in material properties and solution scheme, this example demonstrates the effectiveness of incorporating curl constraints with toolpath-integrated topology optimization for domains in which high fiber curvature is expected. The domain is discretized into 36,000 quadrilateral finite elements with design points defined at the element centroids and 160 CS-RBF support points evenly distributed in a grid over the design domain (blue crossmarks in Fig. 5). The anchor location for ψ_0 is set to coincide with the top left finite element. The prescribed voids (shaded in yellow in Fig. 5) are treated as passive regions in which the density design variables are set to zero at initialization and are not updated during optimization. Numerical parameters specific to the cantilever problems are provided in Table 2.

We begin by designing the cantilever beams without considering any curl constraints and compute the maximum curl value. Next, we impose a curl limit of $\zeta_{\text{all}} = 2\ \text{m}^{-1}$ on the orientation field and show how the structural topologies and fiber towpreg toolpaths change. The first two columns of Fig. 6 show the designs with no curl constraints, where the final topologies are provided in the first column with continuous fiber towpreg toolpaths shown and color maps in the second column denote the absolute value of curl, $|\zeta|$, throughout the structure. Larger values of $|\zeta|$ correspond to higher curvatures in the fiber tows. It is noted that locations with the highest curl in all four designs are typically at locations where towpregs navigate smaller voids since the turning radius of the fiber toolpaths is smaller around voids with smaller radius. The third and fourth columns of Fig. 6 show the final topologies with fiber towpregs toolpaths and color maps denoting the absolute values of curl in the structure, respectively, when curl constraints with a limit of $\zeta_{\text{all}} = 2\ \text{m}^{-1}$ are considered.

For each of the four beams, we observe significant geometric changes in the structural geometries and/or topologies when curl constraints are considered. For the cantilever beam without any prescribed voids (see first row of Fig. 6), the maximum curl in the structure without curl constraints is 8.04 m^{-1} and occurs around the bottom right

Table 1
Numerical parameters common to all design examples.

Parameter	Description	Value
Material properties		
$\hat{E}^m$	Young's modulus of matrix	2.6 GPa
ν_m	Poisson's ratio of matrix	0.3
$\hat{E}_1^f$	Young's modulus of fibers (longitudinal)	131 GPa
$\hat{E}_2^f$	Young's modulus of fibers (transverse)	9 GPa
$\hat{G}_{12}^f$	Shear modulus of fibers	5 GPa
ν_{12}^f	Poisson's ratio of fibers	0.27
Optimization		
Parameter	Description	Value
p	SIMP penalty factor	3
ϵ	Ersatz stiffness	1×10^{-4}
ϱ	Parameter to prevent divide by zero error for CS-RBFs	1×10^{-6}
$\lambda_j^{(0)},\ j = 1, \ldots, N_c$	Initial Lagrange multiplier estimators	15
$\mu^{(0)}$	Initial AL penalty factor	5
$\mu_{\max}$	Maximum AL penalty factor	1×10^{7}
ξ	AL penalty update factor	1.25
η_α	Spatial weighting Heaviside threshold	0.5
`tolD`	Design variable convergence tolerance	0.001
`tolC`	Constraint convergence tolerance	0.005
`MaxIter`	Maximum number of outer loop iterations	200
`MMAIter`	Maximum number of inner MMA[a] iterations	5

[a] The MMA parameters used in all examples for the minimization of the AL function are move=0.15, osc=0.1, asyminit = 0.2, asyminc = 1.2, and asymdecr = 0.7 [44].

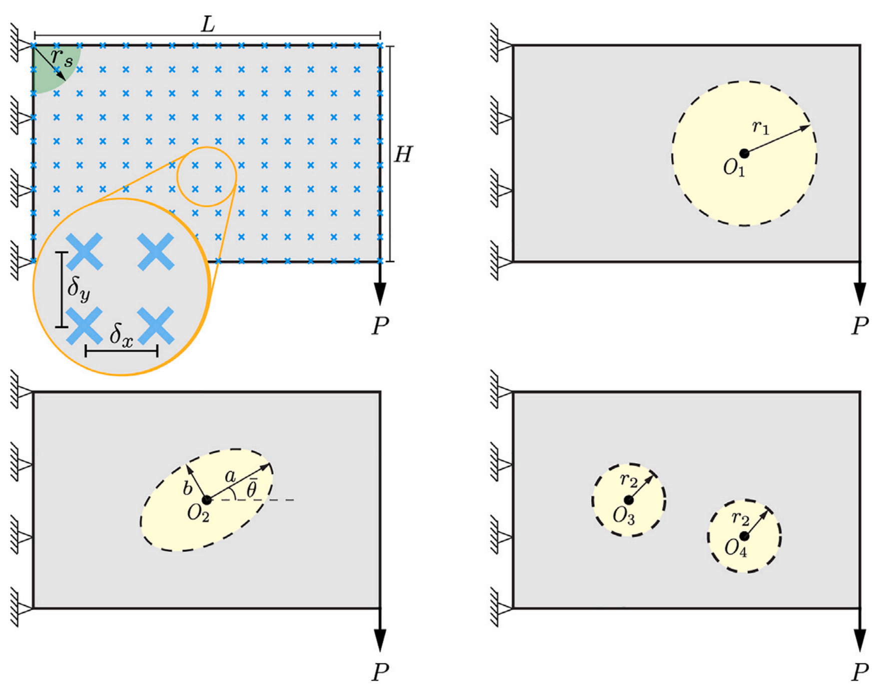

Fig. 5. Design domain and boundary conditions of the four cantilever beams. The CS-RBF support points (denoted by blue crossmarks) and size of their support radius are shown on the leftmost domain. Prescribed voids (passive regions) are indicated in yellow.

void. When we enforce curl constraints, the topology of the structure remains constant, but the size of the voids change to meet the imposed curl limits. For the cantilever beam with a single prescribed circular void (see second row of Fig. 6), the size and shape of the voids change to accommodate the larger turning radius needed to satisfy the curl constraints. Note that the radius of the prescribed circular void in this case is 0.5 m, which corresponds to a curvature of 2 m^{-1}, i.e., the curl limit enforced in this example. In the designs with and without curl constraints, the fiber toolpaths around the prescribed circular void are similar and have a maximum absolute curl of 2 m^{-1}. The third row of Fig. 6 shows the results for the cantilever beam with a prescribed elliptical void. Similarly to the cantilever beam with no prescribed voids, the void causing the highest absolute curl in the structure with no curl constraints changes shape when we enforce curl constraints. Additionally, the strut nearest to the support region disappears when curl constraints are enforced since that member causes an absolute curl of around 7.25 m^{-1}. A similar strut also disappears in the case with two prescribed circular voids (see fourth row of Fig. 6).

The fourth column of Fig. 6 shows that the maximum curl for each design considering curl constraints is equal to ζ_{all}, which indicates that

Table 2
Numerical parameters specific to the cantilever beam design problems.

Parameter	Description	Value
L	Domain length	2.4 m
H	Domain height	1.5 m
O_1	Center of void of cantilever with circular void	(1.6,0.75)
r_1	Radius of void of cantilever with circular void	0.5 m
O_2	Center of void of cantilever with elliptical void	(1.2,0.75)
a	Major axis of ellipse of cantilever with elliptical void	$\frac{1}{2}$ m
b	Minor axis of ellipse of cantilever with elliptical void	$\frac{1}{2\sqrt{3}}$ m
$\bar{\theta}$	Slant angle of ellipse of cantilever with elliptical void	30°
O_3	Center of void of cantilever with two circular voids	(0.8,0.75)
O_4	Center of void of cantilever with two circular voids	(1.6,0.5)
r_2	Radius of voids of cantilever with two circular voids	0.25 m
P	Applied load	0.5 N
R	Filter radius	0.075 m
δ_x	CS-RBF support point horizontal spacing	0.160 m
δ_y	CS-RBF support point vertical spacing	0.167 m
r_s	CS-RBF support radius	0.33 m
v_{all}	Volume limit	0.5
v^f_{all}	Fiber volume limit	0.25
d	Projection spacing factor	0.06
β	Heaviside steepness parameter	100
η	Heaviside threshold	0.5
$z^{(0)}_{\ell}, \ell = 1, \dots, N$	Initial values for density	0.5
$\hat{\theta}^{(0)}_q, q = 1, \dots, M$	Initial values for orientation	0°

the curl constraints are active at some point in the structure. Additionally, the highest curvatures of the final fiber toolpaths, indicated by dotted red lines (see third column of Fig. 6), appear at locations of maximum curl. In fact, the highest curvatures of the fiber toolpaths correspond well with the highest maximum curl values, i.e., $\kappa = \frac{1}{R_s = 0.5\ \text{m}} = 2\text{m}^{-1}$, where R_s is the turning radius of the toolpaths. This observation demonstrates the effectiveness of restricting the curl of the fiber orientation vector field to control the final curvature of the fiber toolpaths generated by the projection method. However, considering curl constraints comes at a cost of degraded mechanical performance, i.e., the objective functions for the designs with curl constraints are higher than those with no manufacturing constraints.

The cantilever beam results are also summarized in Table 3 to highlight the impact on computational cost when curl constraints are considered. The total CPU runtime for each cantilever problem is higher when curl constraints are considered than when no curl constraints are considered. Since more iterations are typically required to achieve convergence in problems with curl constraints, we also compare the runtime per iteration. Problems with curl constraints enforced have a slightly longer runtime per iteration, with an average increase of about 0.17s. This increase in computational cost is modest considering that the proposed method can effectively control local manufacturing constraints related to curl to achieve designs amenable to different CFRP materials and manufacturing techniques.

8.2. Wrench design problem

In this section, we use the wrench design problem to investigate the effect of (1) introducing spatial weighting factors, $\boldsymbol{\alpha}$, to define the gradient of the phase function, $\nabla\boldsymbol{\psi}$ and (2) varying the Heaviside threshold parameter, η, used in projecting the wave function, χ, to distinct material states, $\hat{\chi}$. The design domain and boundary conditions for the wrench problem, adapted from [45], are shown in Fig. 7. The wrench has a load, P, distributed along the bottom half of the left-most circle with center, O_1, and is fixed on the right-most circle with center, O_2. The domain is discretized into 63,000 quadrilateral finite elements with design points defined at the element centroids and 319 CS-RBF support points evenly distributed in a regular grid over the design domain (blue crossmarks in Fig. 7). The anchor location for ψ_0 is set to coincide with the top left finite element. The regions shaded in yellow are treated as passive regions in which the density design variables are set to zero at initialization and are not updated during optimization. Numerical parameters specific to the wrench design problem are provided in Table 4. In the studies associated with the wrench design problem, no manufacturing or fiber volume constraints are considered.

8.2.1. Effect of spatial weighting in the wave projection scheme

Spatial weighting was introduced by Groen and Sigmund [17] to place higher weight on regions of the design containing material than those containing void when calculating the gradient of the phase function (refer to (13)). The rationale for spatial weighting is to promote better alignment between the wave function and the orientation field in material regions. Fig. 8 shows the wrench design without and with considering spatial weighting. In the case with spatial weighting, the Heaviside threshold parameter is $\eta_\alpha = 0.5$. Final topologies with fiber towpregs toolpaths shown are provided in the second row of Fig. 8 and the accompanying color maps, denoting the absolute curl values, $|\zeta|$, throughout the structures are provided in the third row. When spatial weighting is considered, the structural compliance is much lower (3.45 versus 5.11 with and without spatial weighting, respectively) since the wave projection operations do not attempt to align the fiber toolpaths with orientations in the void regions. The curl colormaps also indicate a slight increase in the maximum curl when spatial weighting is considered (20.9 m^{-1} versus 18.8 m^{-1} for the case with and without spatial weighting, respectively), which means that spatial weighting prevents the local curl from being limited indirectly by the wave projection operations, and rather allows them to be controlled more directly by prescribing curl constraints.

8.2.2. Effect of Heaviside projection threshold, η, on final fiber volume

As discussed in Section 4, the Heaviside projection threshold value, η, controls the width of the fiber within a fiber towpreg, where smaller threshold values lead to wider fibers and higher threshold values lead to narrower fibers. As a result, the Heaviside threshold parameter, η, can be used to approximate the total matrix and fiber volume fractions in an optimized structure. For the ideal case in which no fiber curvature is present, the volume fractions of matrix and fiber in the structure would be exactly $v_m = v\eta$ and $v_f = v(1-\eta)$, respectively, where v denotes the volume fraction of composite material, which is typically equal to v_{all}

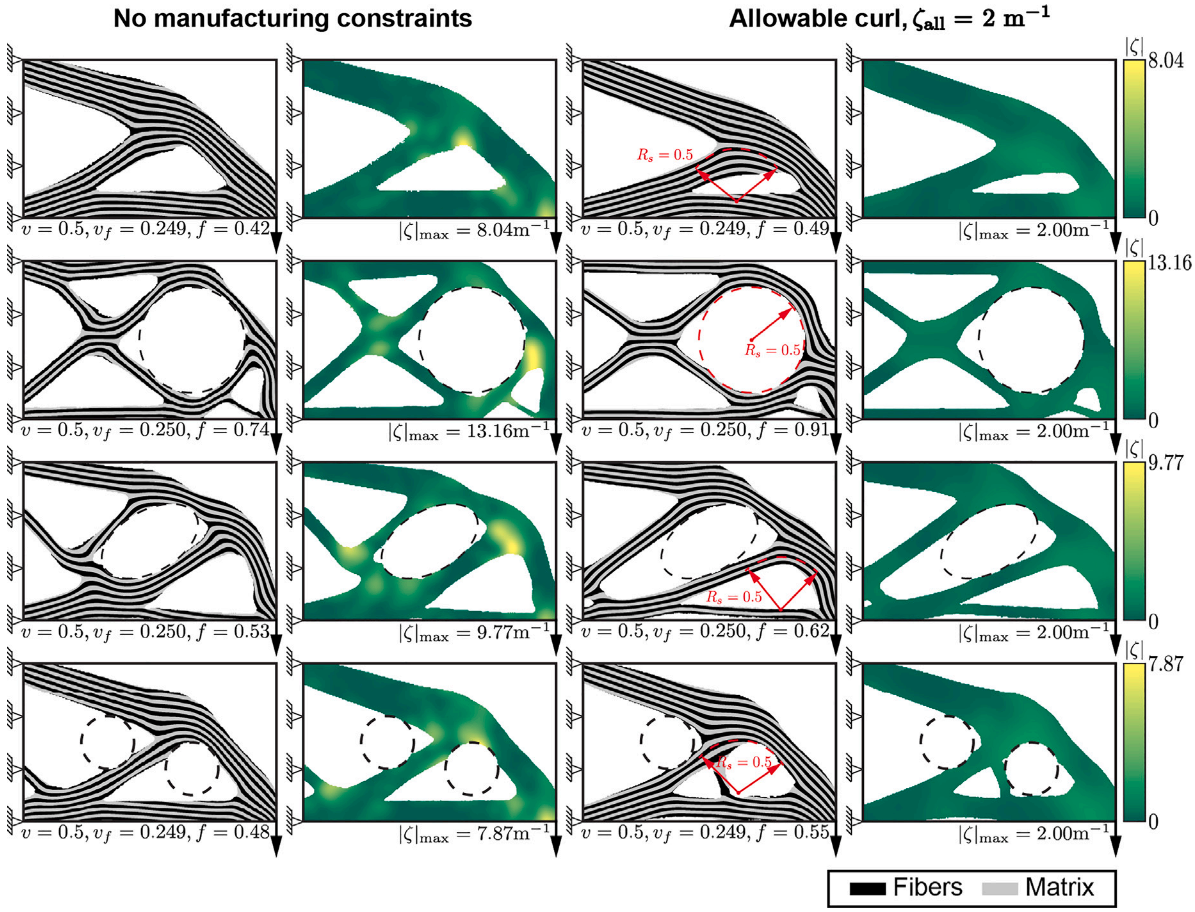

Fig. 6. Cantilever beams optimized with no manufacturing constraints (columns 1 and 2) and with an allowable curl limit of 2 m^{-1} (columns 3 and 4). In both cases, the final topologies with fiber towpregs are shown on the left and the corresponding curl contour map is shown on the right.

Table 3
Objective function value, maximum curl, total CPU runtime, and runtime per iteration for the cantilever beams with and without considering curl constraints.

	No manufacturing constraints				
Design domain	f	$\|\zeta\|_{max}$ (m^{-1})	Time/Iteration	Total number of iterations	Total time
Cantilever	0.42	8.04	2.97	91	270.3
Cantilever (with 1 circular void)	0.74	13.16	2.83	108	305.6
Cantilever (with elliptical void)	0.53	9.77	2.78	102	283.6
Cantilever (with 2 circular voids)	0.48	7.87	2.81	92	258.5
	Allowable curl, ζ_{all}=2 m^{-1}				
	f	$\|\zeta\|_{max}$ (m^{-1})	Time/Iteration	Total number of iterations	Total time
Cantilever	0.49	2	3.15	102	321.3
Cantilever (with 1 circular void)	0.91	2	3.02	118	356.4
Cantilever (with elliptical void)	0.62	2	2.88	109	313.9
Cantilever (with 2 circular voids)	0.55	2	3.01	97	294.9

since the composite volume fraction constraint tends to be active for the volume constrained compliance minimization problem considered here. In this section, we quantify discrepancies between the actual volume fractions and those predicted based on the ideal case.

The results in Fig. 9 show three wrench designs with the same volume fraction of composite material (i.e., $v = v_{\text{all}} = 0.5$), but with different prescribed values of the Heaviside threshold parameter ($\eta = [0.25, 0.5, 0.75]$). With these three values of η, we observe increasing matrix volume fraction ($v_m = [0.14, 0.25, 0.36]$) and decreasing fiber volume fraction ($v_f = [0.36, 0.25, 0.14]$) and note that $v_m/v = [0.28, 0.5, 0.72]$ are close, but not exactly equal to the prescribed η values. As discussed in Section 4, the slight differences are attributed to our inability to precisely control the width of fiber towpregs in the presence of curvature, which causes the fiber towpreg widths to vary along their length. This discrepancy, which is also observed in the study by Ren et al. [15], necessitates additional post-processing steps for current manufacturing processes, such as AFP and MEX, that require constant fiber towpreg width. Nevertheless, η is an effective parameter that that can be used to tune the fiber widths (and fiber/matrix volume fractions) in the design. One additional note on the result in Fig. 9 is that the decrease in fiber

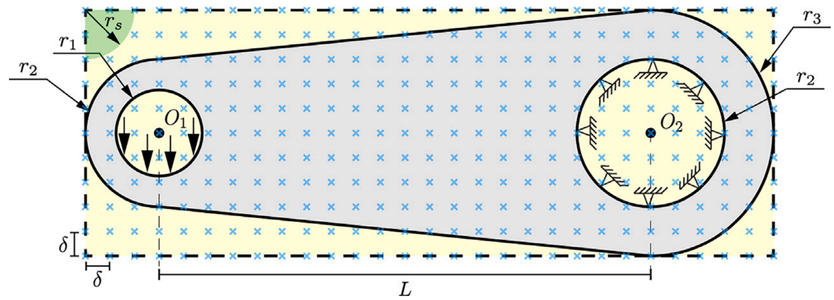

Fig. 7. Design domain and boundary conditions of the wrench design problem with CS-RBF support points (denoted by blue crossmarks) and size of their support radius shown. The regions shaded in yellow are treated as passive regions.

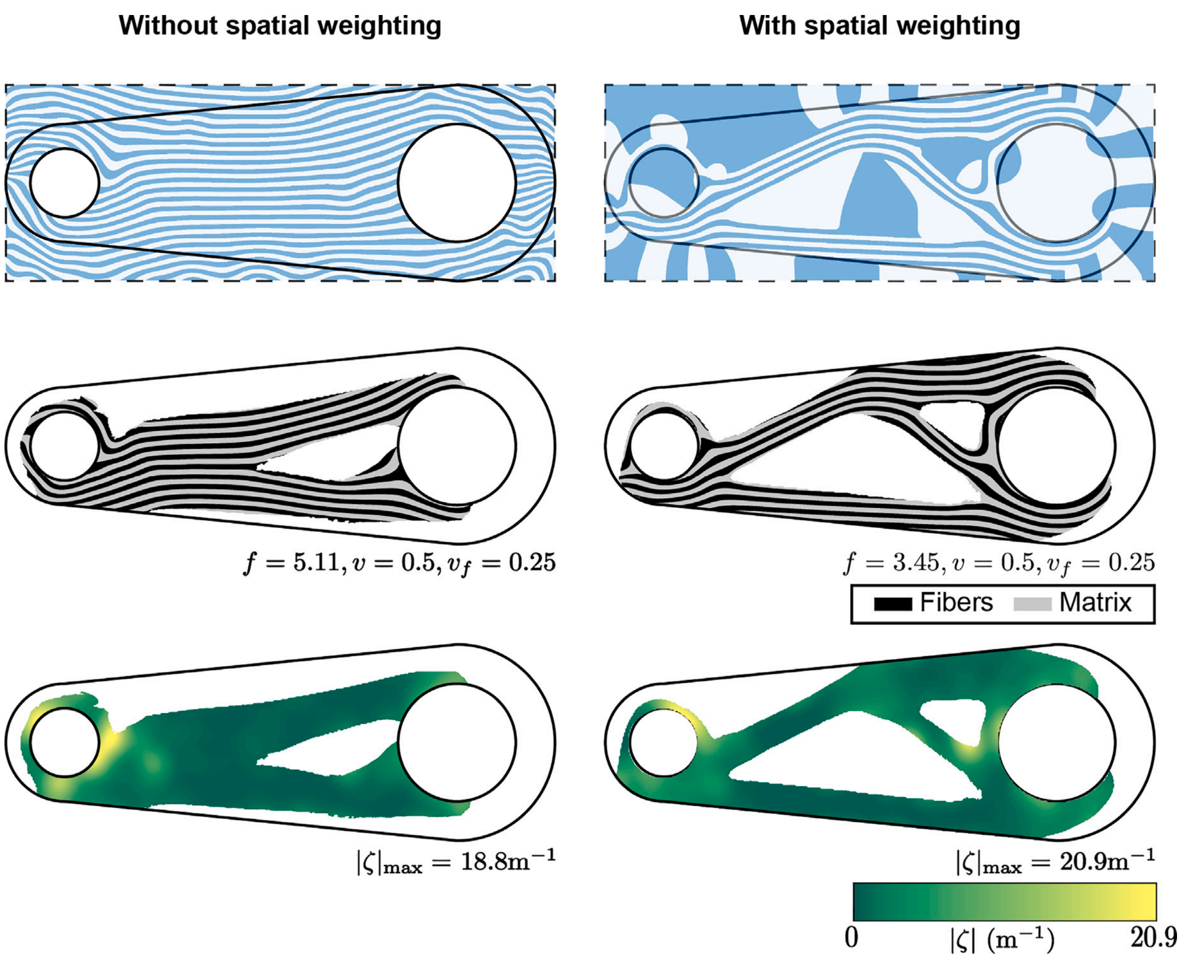

Fig. 8. Optimized wrench design without spatial weighting (left) and with spatial weighting (right). Illustration of the wave projection in the full design domain is shown on the top row. Final topologies and fiber towpreg toolpaths are shown in the middle row and the corresponding curl contour maps are shown on the bottom row. No curl or fiber volume constraints are considered in these designs.

volume and increase in matrix volume is accompanied by an expected increase in structural compliance ($f = [2.74, 3.45, 5.64]$) since the fiber material is stiffer than the matrix material.

8.3. Tuning the wave projection parameters for specific CFRP manufacturing techniques

Recall from Sections 3 and 4 that the wavelength, d, and the Heaviside threshold parameter, η, used in the wave projection operations (see (16) and (17)), can be used to approximate the width of a fiber towpreg and the fiber volume fraction within the fiber towpreg, respectively. As a result, we can use these parameters to achieve physical properties of fiber towpregs needed for different CFRP manufacturing processes. In this section, we use a 2:1 Messerschmitt-Bölkow-Blohm (MBB) beam to show how the optimized design depends on physical properties of the fiber towpregs associated with AFP and MEX. The design domain and boundary conditions are shown in Fig. 10. The domain is discretized into 80,000 quadrilateral finite elements with design points defined at the element centroids and 231 CS-RBF support points defined on a regular grid over the design domain (shown in blue crossmarks in Fig. 10). The anchor location for ψ_0 is set to coincide with the top left finite element. Numerical parameters specific to the 2:1 MBB beam are provided in Table 5.

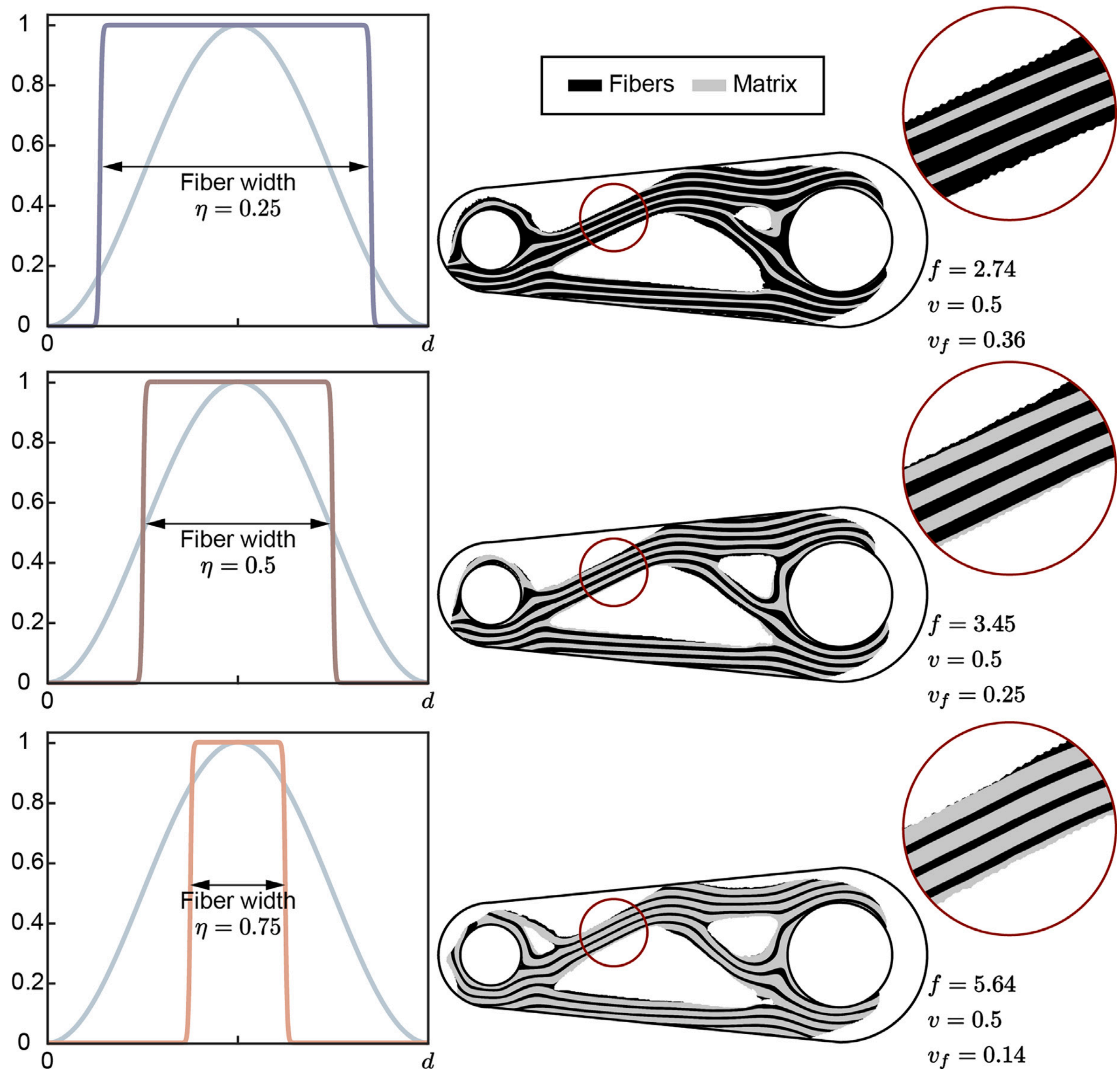

Fig. 9. Optimized wrench designs with increasing Heaviside threshold parameter, η, from top to bottom row. The Heaviside projections of one wavelength are shown on the left. Final topologies with fiber towpregs are shown on the right. No curl fiber volume constraints are considered in these designs.

Table 4
Numerical parameters specific to the wrench design problem.

Parameter	Description	Value
L	Center-to-center distance of circle 1 and circle 2	2 m
P	Applied load	0.6 N
O_1	Center of circle 1	(0.3,0.5)
O_2	Center of circle 2	(2.3,0.5)
r_1	Radius 1	0.175 m
r_2	Radius 2	0.3 m
r_3	Radius 3	0.5 m
R	Filter radius	0.08 m
δ	CS-RBF support point spacing	0.1 m
r_s	CS-RBF support radius	0.2 m
v_{all}	Volume limit	0.5
d	Projection spacing factor	0.07
β	Heaviside steepness parameter	100
$z_\ell^{(0)}, \ell = 1, \dots, N$	Initial values for density	0.5
$\hat{\theta}_q^{(0)}, q = 1, \dots, M$	Initial values for orientation	0°

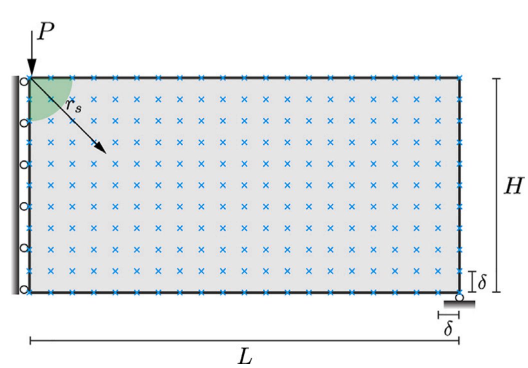

Fig. 10. Design domain and boundary conditions of the 2:1 MBB beam design problem with CS-RBF support points (denoted by blue crossmarks) and size of support radius shown.

Fiber towpregs used in AFP processes are typically 6–13 mm wide and contain 60%–70% fiber [46,47] whereas fiber towpregs used in MEX processes are typically around 1.75 mm wide and contain 25%–35% fiber [48,49]. Here, we define an AFP fiber towpreg with

Table 5
Numerical parameters specific to the 2:1 MBB beam design problem.

Parameter	Description	Value
L	Domain length	20 cm
H	Domain height	10 cm
P	Applied load	0.5 N
R	Filter radius	0.5 cm
δ	CS-RBF support point spacing	1 cm
r_s	CS-RBF support radius	2 cm
v_{all}	Volume limit	0.5
β	Heaviside steepness parameter	100
$z_\ell^{(0)}, \ell = 1,\dots,N$	Initial values for density	0.5
$\hat{\theta}_q^{(0)}, q = 1,\dots,M$	Initial values for orientation	0°

a 10 mm width and a per towpreg fiber volume fraction of 0.6 by setting d = 10 mm and η = 0.4. We also define a MEX fiber towpreg with a 1.5 mm width and a per towpreg fiber volume fraction of 0.35 by setting d = 1.5 mm and η = 0.65. From the toolpaths for each process obtained from the initial guess of the design variables (see second column of Fig. 11), we observe that there are much fewer fiber towpregs for AFP than for MEX since the towpreg width (dictated by d) is much larger for AFP. When we zoom into a small portion of the toolpaths associated with the initial guess, we also observe that the width of the fiber (indicated in black) within each towpreg (indicated in orange) is larger for the towpreg width for AFP than for MEX since the per towpreg fiber volume fraction ($v_{f,\text{tow}} = (1-\eta)$) is larger for AFP. The optimized topologies and fiber toolpaths for the 2:1 MBB beam are shown in the last column of Fig. 11. Both designs contain a composite volume fraction of $v = 0.5$, which is dictated by the composite volume fraction limit, $v_{\text{all}} = 0.5$. As expected, the structure designed with AFP fiber towpregs is more structurally efficient than the one designed with MEX fiber towpregs (structural compliance, f = 0.91 and f = 1.40, for AFP and MEX, respectively) since the AFP towpregs have higher fiber volume fraction (in the ideal case, $v_{f,\text{tow}}$ = 0.6 for AFP and $v_{f,\text{tow}}$ = 0.35 for MEX), which leads to structures with fiber volume fraction, v_f = 0.29 and v_f = 0.19 for AFP and MEX, respectively. Once again, due to towpreg curvature, fiber volume fraction relative to the volume of composite in the final structure, i.e., v_f/v = 0.58 for AFP and $v_f/v = 0.38$ for MEX), are close, but not exactly equal to the per towpreg fiber volume fractions, $v_{f,\text{tow}}$ = 0.6 and $v_{f,\text{tow}}$ = 0.35 expected for the no curvature cases of AFP and MEX, respectively. This example demonstrates the usefulness of the proposed formulation in considering the physical attributes of fiber towpregs used in different manufacturing processes, and it allows us to design CFRPs that are amenable to different manufacturing processes.

Additionally, in actual manufacturing of CFRPs, it is known that the MEX process has more flexibility in manufacturing finer features due to the smaller towpregs. Interestingly, we observe thinner strut members and finer features in the optimized topology of MEX-towpreg design, which can be attributed to the smaller width, defined by d.

8.4. *Comparison of toolpath generation during topology optimization versus in post-processing*

Toolpath-integration was first introduced to density-based topology optimization by Ren et al. [15] in an effort to promote better agreement between fiber toolpaths and the discrete fiber orientations obtained from topology optimization than can be achieved using post-processing approaches that rely on computational homogenization to model the material properties of CFRPs. In this section, we compare the proposed toolpath-integrated topology optimization formulation considering curl constraints with the author's previous formulation that requires the toolpath to be generated during post-processing [7]. We note that because the formulation requiring post-processing also makes use of CS-RBFs, many of the issues related to fiber path intersections and discontinuities observed by Ren et al. [15] in post-processing approaches

Table 6
Numerical parameters specific to the 3:1 MBB beam design problem.

Parameter	Description	Value
L	Domain length	3 m
H	Domain height	1 m
P	Applied load	0.5 N
R	Filter radius	0.1 m
δ	CS-RBF support point spacing	0.25 m
r_s	CS-RBF support radius	0.5 m
v_{all}	Volume limit	0.5
v_{all}^f	Fiber volume limit	0.25
d	Projection spacing factor	0.03
β	Heaviside steepness parameter	100
η	Heaviside threshold	0.5
$z_\ell^{(0)}, \ell = 1,\dots,N$	Initial values for density	0.5
$\hat{\theta}_q^{(0)}, q = 1,\dots,M$	Initial values for orientation	0°

do not appear here. We use a 3:1 MBB beam to compare the final designs and computational cost associated with each approach. The design domain and boundary conditions of the 3:1 MBB beam are shown in Fig. 12. The domain is discretized into 30,000 quadrilateral finite elements with design points defined at the element centroids and 65 CS-RBF points evenly distributed in a regular grid over the design domain. Parameters specific to the 3:1 MBB beam are provided in Table 6.

The formulation requiring toolpath generation during post-processing is very similar to that proposed here, except that it skips the "toolpath generation" step in Fig. 4 (i.e., the wave projection procedure described in Section 3). Thus, rather than defining properties of fiber and matrix explicitly according to a toolpath, properties of the composite are approximated during topology optimization directly from the fiber orientation field using homogenization. We refer the reader to Wong et al. [7] for specific details of the post-processing formulation and only highlight a few minor changes here that promote a more fair comparison with the current toolpath-integrated approach. First, instead of using Mori–Tanaka homogenization to approximate the composite properties during topology optimization, as was done by Wong et al. [7], we use the analytical homogenized properties presented by Gibson [33] to predict the stiffness elasticity tensor of a two-phase anisotropic fiber composite material, i.e.,

$$\hat{\mathbf{D}}^H = \begin{bmatrix} \frac{E_1}{1-\nu_{12}\nu_{21}} & \frac{\nu_{12}E_2}{1-\nu_{12}\nu_{21}} & 0 \\ \frac{\nu_{12}E_2}{1-\nu_{12}\nu_{21}} & \frac{E_2}{1-\nu_{12}\nu_{21}} & 0 \\ 0 & 0 & G_{12}. \end{bmatrix}, \tag{53}$$

where the analytical expressions for E_1, E_2, ν_{12} and G_{12} are

$$\begin{aligned} E_1 &= \hat{E}_{f1} v_f + \hat{E}_m v_m, \\ E_2 &= \hat{E}_m \left[(1-\sqrt{v_f}) + \frac{\sqrt{v_f}}{1-\sqrt{v_f}(1-\frac{\hat{E}_m}{E_{f2}})} \right], \\ \nu_{12} &= \nu_{12} v_f + \nu_m v_m, \quad \text{and} \\ G_{12} &= \hat{G}_m \left[(1-\sqrt{v_f}) + \frac{\sqrt{v_f}}{1-\sqrt{v_f}(1-\frac{\hat{G}_m}{G_{12}})} \right], \end{aligned} \tag{54}$$

respectively [33]. In (54), v_f and v_m denote the fiber and matrix volume fractions, respectively, and are defined as 0.5 in this example. The global stiffness matrix is assembled from the local element stiffness matrices, i.e., $(\mathbf{k}_\ell^0)_{jk} = \int_{\Omega_\ell} \mathbf{B}_j{}^T \mathbf{D}_\ell^H(\theta_\ell) \mathbf{B}_k d\Omega_\ell$, $\ell = 1,\dots,N$ with $\mathbf{D}_\ell^H(\theta_\ell) = \mathbf{T}(\theta_\ell)\hat{\mathbf{D}}^H\mathbf{T}(\theta_\ell)^T$. A second deviation from the approach presented by Wong et al. [7] is that rather than using a streamline method to generate the final fiber towpregs in post-processing, for fair comparison, we adopt the wave projection technique discussed in Section 3.

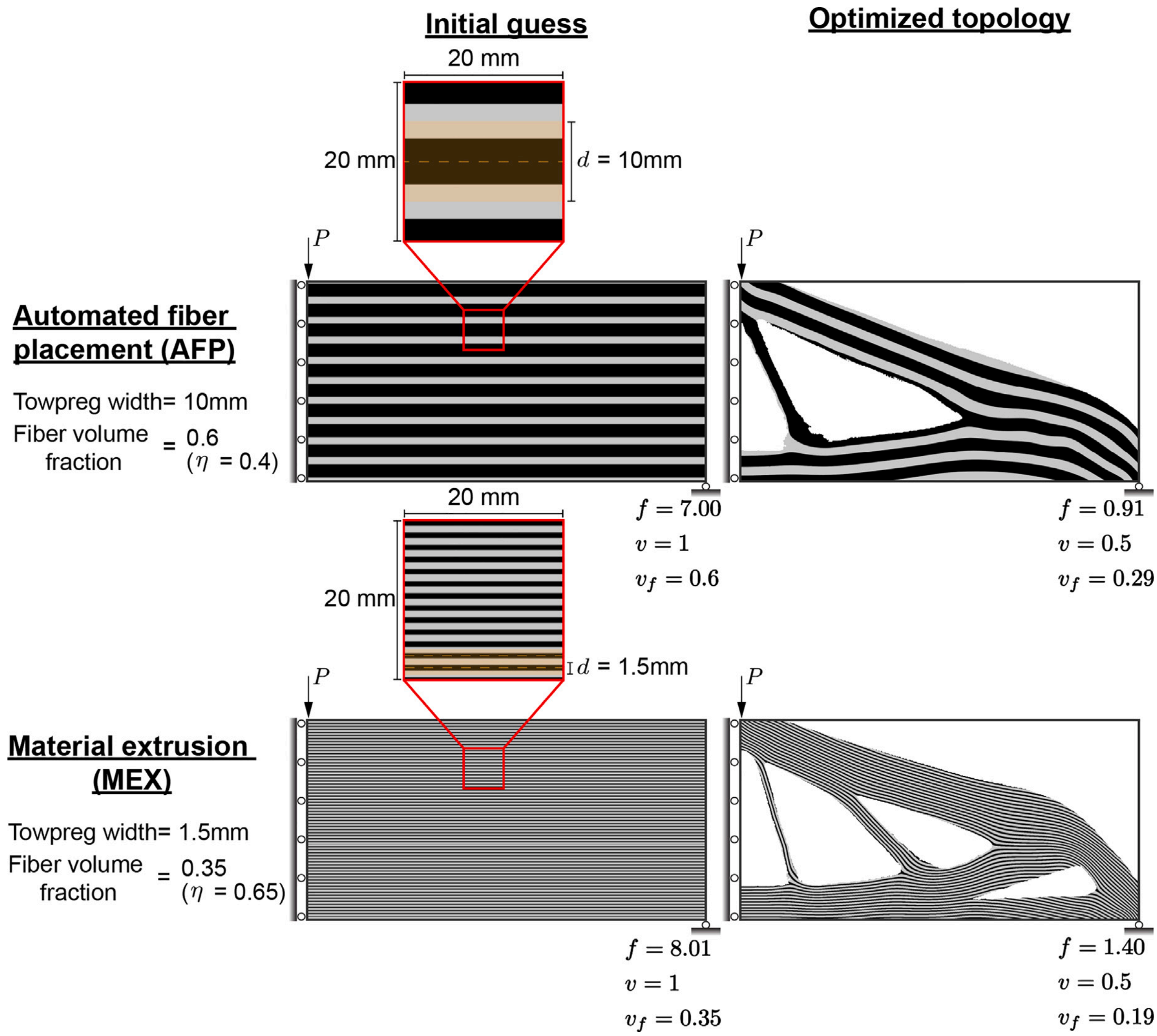

Fig. 11. 2:1 MBB beam designed considering the AFP process (top) and the MEX process (bottom). The initial guess of each design problems is shown in the second column and final topologies with fiber towpregs are shown in the last column. No curl or fiber volume constraints are considered in these designs.

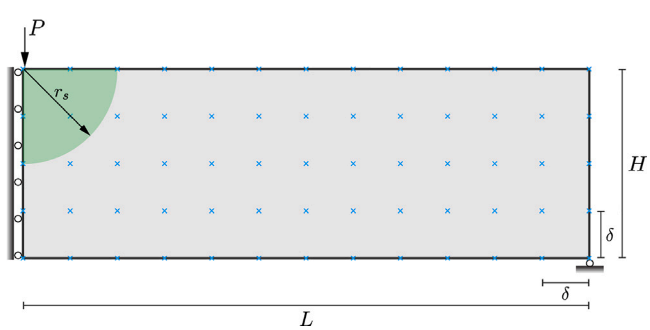

Fig. 12. Design domain and boundary conditions of the 3:1 MBB beam design problem with CS-RBF support points (denoted by blue crossmarks) and size of support radius shown.

We use both the proposed toolpath-integrated approach and the approach requiring post-processing to design the 3:1 MBB beam without any curl constraints and with allowable curl limits of $\zeta_{\text{all}} = 1$ m^{-1} and $\zeta_{\text{all}} = 0.1$ m^{-1}. In the post-processing method, the fiber toolpaths are generated using the same wave projection parameters (d, β, η) used in the toolpath-integrated approach (see Table 6), and we recompute the objective function value after post-processing based on the material state (i.e., the element stiffness matrices in the final analysis are computed using (10)). The final topologies with fiber toolpaths shown, as well as colormaps of the local curl distribution, are provided for each case in Fig. 13. In the toolpath-integrated approach, the maximum curl in the structure without curl constraints is 6.01 m^{-1} and the structural compliance, $f = 1.97$. This result is very similar to the post-processed design, where the maximum curl is 6.51 m^{-1} and the structural compliance, $f = 1.90$. As we enforce curl constraints with progressively tighter limits, the voids change shape and size in a similar way for both methods until we arrive at a two-strut structure when $\zeta_{\text{all}} = 0.1$ m^{-1}. The maximum curl in each curl-constrained design is equal to ζ_{all}, which indicates that the curl constraints are active at some point in the structure for both methods. Additionally, the structural compliance values increase with stricter curl limits and are almost identical between the two methods.

The results of the 3:1 MBB beam are also summarized in Table 7 for the two approaches, where computational cost is reported. The runtime per iteration and total runtime of the post-processing method

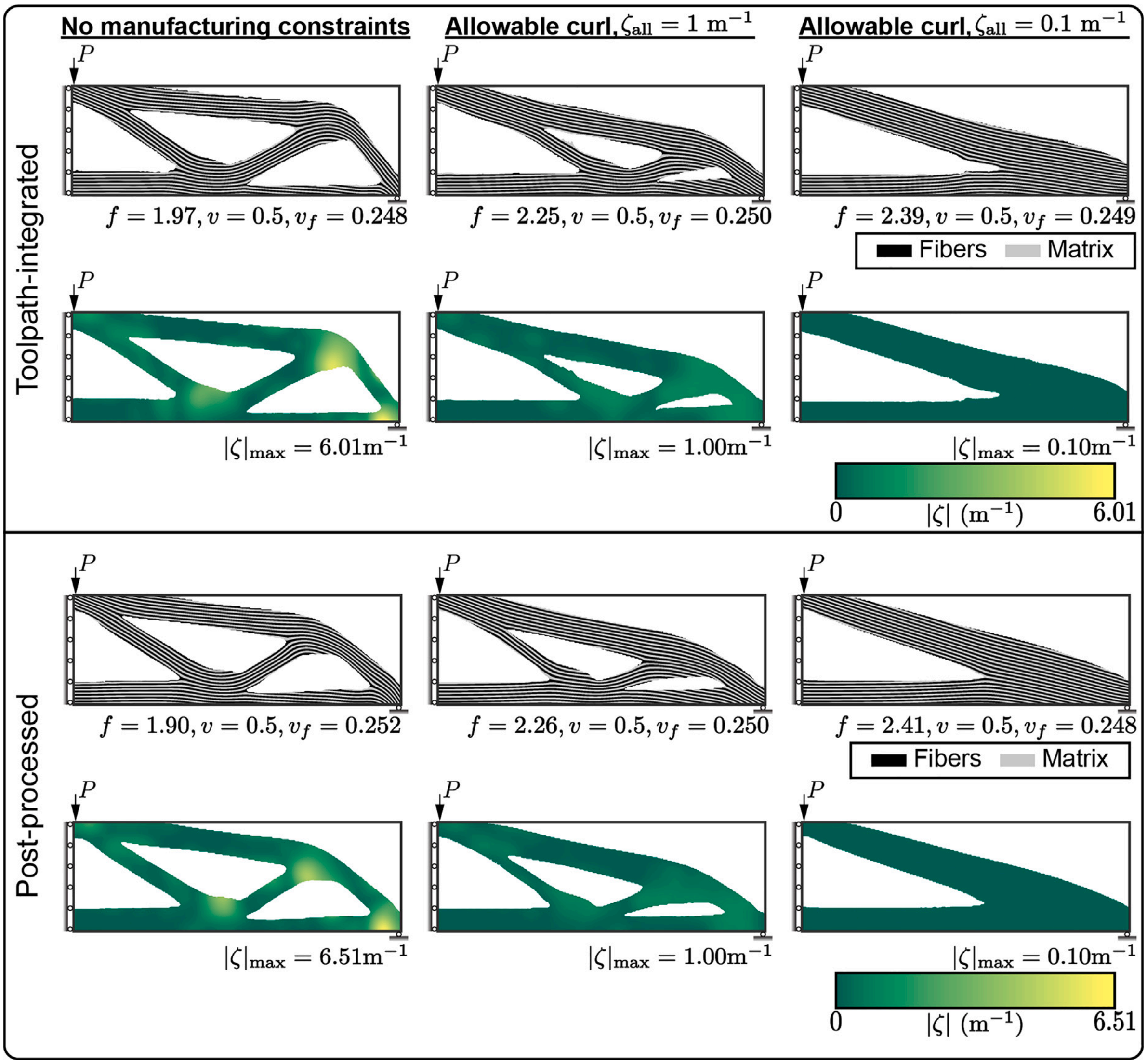

Fig. 13. 3:1 MBB beam designed with decreasing curl limits from left to right using the proposed toolpath-integrated topology optimization formulation (top) and a formulation requiring post-processing for toolpath generation (bottom). For each approach, final topologies with fiber towpregs and the corresponding curl contour map are shown.

are always lower than those of the toolpath-integrated approach. The significant increase in runtime per iteration (195%, 91.5% and 105.4% for no curl constraints, $\zeta_{all} = 1\ m^{-1}$, and $\zeta_{all} = 0.1\ m^{-1}$, respectively) when using the toolpath-integrated approach as compared to the post-processing approach is attributed to generating the fiber toolpaths in each iteration. The main computational bottleneck lies in calculating the phase in (15) and its associated sensitivities in (37). The post-processing time in the post-processing approach includes generating the toolpath, performing an additional finite element analysis based on the post-processed material state, and recalculating the structural compliance. These steps take an average of 68 s. When the post-processing time is considered together with the total runtime for optimization, the total time for the post-processing approach still remains lower than that of the toolpath-integrated approach. Note that the total runtimes of the two methods become closer as we enforce a tighter curl limit since the post-processing approach requires more iterations to reach convergence with tighter limits of curl constraints.

The observed reduction in computational efficiency associated with integrating toolpath generation into the topology optimization loop is expected, and the results reported in Fig. 13 and Table 7 indicate that there is not enough gain in accuracy (no gain) to justify the additional computational cost. However, d was selected for the results in Fig. 13 and Table 7 such that the length scale of fiber towpregs were small enough to be well-represented by homogenized properties. The toolpath integrated approach provides additional freedom to vary the physical properties of the fiber towpregs in accordance with manufacturing requirements, which is not possible in the post-processing approach. To demonstrate this point, Fig. 14 shows the final topologies with toolpath and colormaps of their curl distributions for $d = [0.03, 0.04, 0.06]$ m (without curl constraints), considering both the toolpath-integrated and post-processing approaches. Notice that the topology is identical for each design from the post-processing approach since it relies on homogenized properties that assume the fiber towpreg microstructures are infinitely small relative to the macroscale structure. Differences in the designs from the post-processing approach are introduced only when the toolpath is generated and since the homogenized properties do not represent the true CFRP properties well, we notice degraded structural performance relative to the design obtained using the toolpath-integrated approach. It is expected that the toolpath-integrated approach will have benefits in other problems with manufacturing limits that require an explicit representation of the fiber–matrix distribution (e.g., minimum fiber length).

Table 7
Comparison of the objective function, maximum curl and runtime for the 3:1 MBB beam example considering curl constraints of the toolpath-integrated and post-processed approaches.

	Toolpath-integrated						
ζ_{all} (m^{-1})	f^H	f	$\lvert\zeta\rvert_{\max}$ (m^{-1})	Number of iterations	Time/iteration	Postprocessing time	Total runtime
–	–	1.97	6.01	127	2.19	–	278.33
1	–	2.25	1.00	135	2.25	–	303.90
0.1	–	2.39	0.10	153	2.30	–	351.90
	Post-processed						
	f^H	f	$\lvert\zeta\rvert_{\max}$ (m^{-1})	Number of iterations	Time/iteration	Postprocessing time	Total runtime
–	1.22	1.90	6.51	74	0.74	65.50	120.40
1	1.52	2.26	1.00	128	1.18	69.90	221.00
0.1	1.69	2.41	0.10	227	1.12	66.80	321.00

[a] f^H is the structural compliance of the post-processed method before recalculation of the structural compliance after fiber towpreg toolpaths are generated.

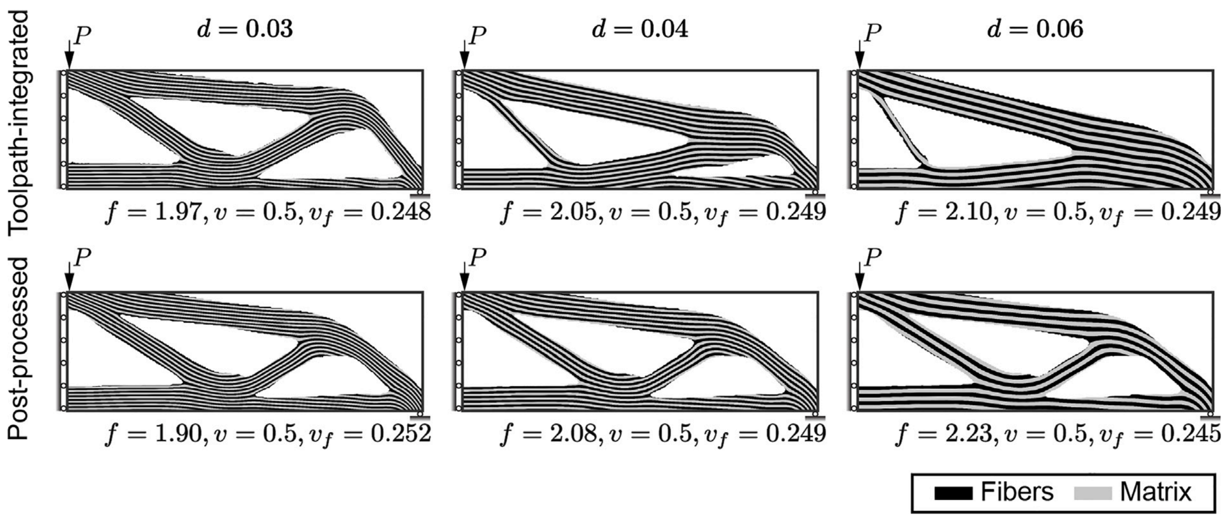

Fig. 14. 3:1 MBB beam designed using the proposed toolpath-integrated approach (top) and a post-processed approach (bottom) with increasing towpreg width (controlled by d) from left to right. Final topologies with fiber towpregs are shown. No curl constraints are considered in these designs.

9. Conclusion

We proposed a toolpath-integrated topology optimization formulation for volume-constrained compliance minimization of structures composed of CFRPs considering manufacturing constraints on fiber layout, in order to balance structural performance, material use, and manufacturability. The proposed formulation is the first density-based approach to consider fiber layout constraints together with toolpath generation in the optimization loop. The former reduces deviations between the as-designed and as-manufactured fiber layout while the latter promotes a more accurate representation of the CFRP mechanical properties during the design process. The local curl constraints, which limit fiber towpreg curvature, are facilitated by defining discrete fiber orientation design variables on CS-RBFs that ensure continuity needed for taking derivatives of the constraints. Toolpath generation is accomplished using a wave projection that transforms the discrete orientation design variables into manufacturable fiber toolpaths defined by distinct fiber or matrix material states at each design point. Together, the fiber layout constraints and integrated toolpath generation scheme lead to optimized CFRP structures in which the mechanical behavior expected from the designed part can be achieved more closely upon manufacturing. In fact, we demonstrated that curl constraints can be defined based on curvature limits associated with a specific CFRP manufacturing process and parameters of the wave projection can be used to tune dimensions of fiber towpregs needed for different CFRP manufacturing processes. As a result, optimized designs obtained from the proposed method differ depending on the manufacturing process of interest.

The toolpath-integrated approach proposed here has great potential for problems in which an explicit representation of the CFRP is needed (e.g., those considering buckling or stress limits). Additionally, in some CFRP manufacturing processes (e.g., AFP) a minimum fiber towpreg cut length is dictated by the distance of the spool storing the fiber towpreg and the cutting mechanism of the machine. In some of the designs obtained from the proposed toolpath-integrated topology optimization approach, we observed regions where the final fiber towpreg length may not meet the minimum required by AFP. Because the fiber towpregs are explicitly-modeled in the proposed toolpath-integrated approach, additional constraints on fiber towpreg length could be enforced as an extension of the current method.

CRediT authorship contribution statement

Janet Wong: Writing – review & editing, Writing – original draft, Visualization, Validation, Methodology, Investigation, Formal analysis, Data curation, Conceptualization. **Emily D. Sanders:** Writing – review & editing, Supervision, Conceptualization. **David W. Rosen:** Writing – review & editing, Supervision, Conceptualization.

Replication of results

The numerical results presented in this document can be replicated using the methodology and formulations described here.

Declaration of competing interest

The authors declare the following financial interests/personal relationships which may be considered as potential competing interests: Janet Wong reports financial support was provided by DSO National Laboratories. If there are other authors, they declare that they have no known competing financial interests or personal relationships that could have appeared to influence the work reported in this paper.

Acknowledgment

JW was supported by the DSO postgraduate scholarship from DSO National Laboratories, Singapore. EDS acknowledges startup support from George W. Woodruff School of Mechanical Engineering. DWR acknowledges support from his A*STAR start-up fund. Any opinions, findings and conclusions expressed in this paper are those of the authors(s) and do not necessarily reflect the views of the sponsoring agencies.

Data availability

Data will be made available on request.

References

[1] Boddeti Narasimha, Tang Yunlong, Maute Kurt, Rosen David W, Dunn Martin L. Optimal design and manufacture of variable stiffness laminated continuous fiber reinforced composites. Sci Rep 2020;10(1):16507.
[2] Papapetrou Vasileios S, Patel Chitrang, Tamijani Ali Y. Stiffness-based optimization framework for the topology and fiber paths of continuous fiber composites. Compos Part B: Eng 2020;183:107681.
[3] Shafighfard Torkan, Cender Thomas A, Demir Eralp. Additive manufacturing of compliance optimized variable stiffness composites through short fiber alignment along curvilinear paths. Addit Manuf 2021;37:101728.
[4] Kim Dongjin, Lee Jaewook, Nomura Tsuyoshi, Dede Ercan M, Yoo Jeonghoon, Min Seungjae. Topology optimization of functionally graded anisotropic composite structures using homogenization design method. Comput Methods Appl Mech Engrg 2020;369:113220.
[5] Liu Tong, Yuan Shangqin, Wang Yaohui, Xiong Yi, Zhu Jihong, Lu Lu, Tang Yunlong. Stress-driven infill mapping for 3D-printed continuous fiber composite with tunable infill density and morphology. Addit Manuf 2023;62:103374.
[6] Wang Ting, Li Nanya, Link Guido, Jelonnek John, Fleischer Jürgen, Dittus Jörg, Kupzik Daniel. Load-dependent path planning method for 3D printing of continuous fiber reinforced plastics. Compos Part A: Appl Sci Manuf 2021;140:106181.
[7] Wong Janet, Sanders Emily D, Rosen David W. Topology optimization of additively manufactured continuous fiber-reinforced structures with constraints on fiber path geometry. Struct Multidiscip Optim 2025;68(5):1–29.
[8] Sun Bing, Xing Yue, Lv Pengyu, Zhou Jin, Liu Chunqi, Duan Huiling, Liang Xiubing. Concurrent optimization of continuous carbon fiber-reinforced composites with multi-scale components considering the manufacturing constraint. Compos Sci Technol 2025;259:110942.
[9] Liu Jikai, Yu Huangchao. Concurrent deposition path planning and structural topology optimization for additive manufacturing. Rapid Prototyp J 2017;23(5):930–42.
[10] Xu Yanan, Gao Yunkai, Wu Chi, Fang Jianguang, Sun Guangyong, Steven Grant P, Li Qing. Concurrent optimization of topological configuration and continuous fiber path for composite structures—A unified level set approach. Comput Methods Appl Mech Engrg 2022;399:115350.
[11] Pradhan Arijit, Boddeti Narasimha. Multiscale topology optimization of architected fiber reinforced composites considering manufacturability. Comput Methods Appl Mech Engrg 2025;444:118121.
[12] Mokhtarzadeh Mohammad, López Jiménez Francisco, Maute Kurt. Concurrent level set topology and fiber orientation optimization of fiber-reinforced composite structures. Struct Multidiscip Optim 2024;67(7):117.
[13] Li Guixing, Chen Yuan. Highly efficient and extensible parallel topology optimization for continuous fiber reinforced composites. Comput Methods Appl Mech Engrg 2025;436:117713.
[14] Li Hang, Gao Liang, Li Hao, Li Xiaopeng, Tong Haifeng. Full-scale topology optimization for fiber-reinforced structures with continuous fiber paths. Comput Methods Appl Mech Engrg 2021;377:113668.
[15] Ren Huilin, Wang Dan, Liu Guang, Rosen David W, Xiong Yi. Concurrent optimization of structural topology and toolpath for additive manufacturing of continuous fiber-reinforced polymer composites. Comput Methods Appl Mech Engrg 2024;430:117227.
[16] Pantz Olivier, Trabelsi Karim. A post-treatment of the homogenization method for shape optimization. SIAM J Control Optim 2008;47(3):1380–98.
[17] Groen Jeroen P, Sigmund Ole. Homogenization-based topology optimization for high-resolution manufacturable microstructures. Internat J Numer Methods Engrg 2018;113(8):1148–63.
[18] Fernandez Felipe, Compel W Scott, Lewicki James P, Tortorelli Daniel A. Optimal design of fiber reinforced composite structures and their direct ink write fabrication. Comput Methods Appl Mech Engrg 2019;353:277–307.
[19] Guo Huiqiang, Li Zhengguang, Bai Jiantao, Zhang Ran, Zuo Wenjie. Continuous fiber paths optimization for composite structures with stress and manufacturing constraints using a parametric level set method. Acta Mech Sin 2026;42(4):424849.
[20] Guo Huiqiang, Wang Jing, Li Zhengguang, Zuo Wenjie, Bai Jiantao. Fiber path optimization of geometric nonlinear composite structures using a parametric level set method. Eur J Mech A Solids 2025;105769.
[21] Bruns Tyler E, Tortorelli Daniel A. Topology optimization of non-linear elastic structures and compliant mechanisms. Comput Methods Appl Mech Engrg 2001;190(26–27):3443–59.
[22] Kiyono César Yukishigue, Silva Emílio Carlos Nelli, Reddy JN. A novel fiber optimization method based on normal distribution function with continuously varying fiber path. Compos Struct 2017;160:503–15.
[23] Luo Chuan, Ferrari Federico, Guest James K. Design optimization of advanced tow-steered composites with manufacturing constraints. Compos Part B: Eng 2024;284:111739.
[24] Nocedal Jorge, Wright Stephen J. Numerical optimization. 2nd ed. Springer Berlin; 2006.
[25] Bertsekas Dimitri P. Constrained optimization and Lagrange multiplier methods. 1st ed. Athena Scientific; 1996.
[26] Bourdin Blaise. Filters in topology optimization. Internat J Numer Methods Engrg 2001;50(9):2143–58.
[27] Borrvall Thomas, Petersson Joakim. Topology optimization using regularized intermediate density control. Comput Methods Appl Mech Engrg 2001;190:4911–28.
[28] Bendsøe Martin P. Optimal shape design as a material distribution problem. Struct Optim 1989;1(4):193–202.
[29] Zhou Ming, Rozvany George IN. The COC algorithm, Part II: Topological, geometrical and generalized shape optimization. Comput Methods Appl Mech Engrg 1991;89(1–3):309–36.
[30] Wendland Holger. Piecewise polynomial, positive definite and compactly supported radial functions of minimal degree. Adv Comput Math 1995;4:389–96.
[31] Wei Peng, Li Zuyu, Li Xueping, Wang Michael Yu. An 88-line Matlab code for the parameterized level set method based topology optimization using radial basis functions. Struct Multidiscip Optim 2018;58:831–49.
[32] Rumpf Raymond C, Pazos Javier. Synthesis of spatially variant lattices. Opt Express 2012;20(14):15263–74.
[33] Gibson Ronald F. Principles of composite material mechanics. CRC Press; 2007.
[34] Altassan Abdulmajeed, Wang Leyi, Sanders Emily. PolyAnisoMat: An efficient matlab code for multi-anisotropic-material topology optimization with spatially-variable relative density and orientation. 2025 [submitted for publication].
[35] Noble Ben, Daniel James W. Applied linear algebra. vol. 3, NJ: Prentice-Hall Englewood Cliffs; 1977.
[36] Greifenstein Jannis, Stingl Michael. Simultaneous parametric material and topology optimization with constrained material grading. Struct Multidiscip Optim 2016;54:985–98.
[37] Jensen Peter Dørffler Ladegaard, Sigmund Ole, Groen Jeroen P. Dehomogenization of optimal 2D topologies for multiple loading cases. Comput Methods Appl Mech Engrg 2022;399:115426.
[38] Nomura Tsuyoshi, Dede Ercan M, Lee Jaewook, Yamasaki Shintaro, Matsumori Tadayoshi, Kawamoto Atsushi, Kikuchi Noboru. General topology optimization method with continuous and discrete orientation design using isoparametric projection. Internat J Numer Methods Engrg 2015;101(8):571–605.
[39] Schmidt Martin-Pierre, Couret Laura, Gout Christian, Pedersen Claus BW. Structural topology optimization with smoothly varying fiber orientations. Struct Multidiscip Optim 2020;62(6):3105–26.
[40] Brooks Timothy R, Martins Joaquim RRA. On manufacturing constraints for tow-steered composite design optimization. Compos Struct 2018;204:548–59.
[41] Ding Haoqing, Xu Bin. A novel discrete–continuous material orientation optimization model for stiffness-based concurrent design of fiber composite. Compos Struct 2021;273:114288.
[42] Senhora Fernando V, Giraldo-Londono Oliver, Menezes Ivan FM, Paulino Glaucio H. Topology optimization with local stress constraints: A stress aggregation-free approach. Struct Multidiscip Optim 2020;62:1639–68.

[43] Giraldo-Londoño Oliver, Paulino Glaucio H. PolyStress: A Matlab implementation for local stress-constrained topology optimization using the augmented Lagrangian method. Struct Multidiscip Optim 2021;63(4):2065–97.
[44] Svanberg Krister. The method of moving asymptotes—a new method for structural optimization. Internat J Numer Methods Engrg 1987;24(2):359–73.
[45] Talischi Cameron, Paulino Glaucio H, Pereira Anderson, Menezes Ivan FM. PolyTop: a Matlab implementation of a general topology optimization framework using unstructured polygonal finite element meshes. Struct Multidiscip Optim 2012;45(3):329–57.
[46] Carosella Stefan, Hügle Sebastian, Helber Florian, Middendorf Peter. A short review on recent advances in automated fiber placement and filament winding technologies. Compos Part B: Eng 2024;111843.
[47] Wagmare Rajkumar, Harshe Rahul, Pednekar Jaising, Patro T Umasankar. Additive manufacturing of continuous fiber-reinforced polymer composites: Current trend and future directions. Prog Addit Manuf 2024;1–28.
[48] Kabir SM Fijul, Mathur Kavita, Seyam Abdel-Fattah M. A critical review on 3D printed continuous fiber-reinforced composites: History, mechanism, materials and properties. Compos Struct 2020;232:111476.
[49] Karimi Armin, Rahmatabadi Davood, Baghani Mostafa. Various FDM mechanisms used in the fabrication of continuous-fiber reinforced composites: A review. Polymers 2024;16(6):831.